

Ambient Noise Analyses at Broadband Ocean-Bottom Seismometers: Data Quality and Transfer Function Corrections

Helen A. Janiszewski^{*1}  and Joshua B. Russell² 

Abstract

Seismic ambient noise tomography has revolutionized regional crustal and upper-mantle imaging for broadband ocean-bottom seismometer (BBOBS) studies. However, the ocean poses unique challenges including tilt and compliance noise, and interface waves with considerable water-column sensitivity. Transfer function (TF) noise removal techniques enable separation of fundamental Scholte waves from overtone Rayleigh waves, but such noise removal strategies do not always provide the expected signal improvement. Here, we leverage data from recent U.S.-led BBOBS deployments to evaluate variability in ambient-noise surface-wave quality and efficacy of TF corrections across different oceanic environments and instrumentation. We examine the 15–30 and 3–10 s period bands that are typically used in lithospheric imaging. We find that water depth, sediment thickness, instrument design, and ocean basin characteristics are the primary factors influencing ambient-noise data quality and effectiveness of TF corrections. In the 3–10 s period band, enhancement of higher-mode Rayleigh waves is most successful in deep waters with thin sediments. In the 15–30 s period band, signal is improved both in shallow waters likely due to infragravity wave removal, and in instances of high tilt noise. Our results provide new insights into the environmental conditions and instrument designs that shape ambient noise tomography performance, offering practical guidance for optimizing future BBOBS studies as well as novel seafloor-sensing technologies.

Cite this article as Janiszewski, H. A., and J. B. Russell (2025). Ambient Noise Analyses at Broadband Ocean-Bottom Seismometers: Data Quality and Transfer Function Corrections, *Seismol. Res. Lett.*, **XX**, 1–19, doi: [10.1785/0220250106](https://doi.org/10.1785/0220250106).

Supplemental Material

Introduction

In the past two decades, seismic ambient noise tomography has become a useful tool for imaging regional crustal and upper-mantle structure (Shapiro and Campillo, 2004). The increasing availability of broadband ocean-bottom seismometer (BBOBS) data has enabled the expansion of ambient noise tomography in marine environments (Harmon *et al.*, 2007; Takeo *et al.*, 2014; Lin *et al.*, 2016; Russell *et al.*, 2019). This method relies on cross correlations of continuous seismic recordings between stations to estimate empirical Green's functions, and it is well suited for the oceans where the microseism sources are strongest. Marine studies provide some of the highest quality images of the lithospheric mantle, partly due to the relatively thin, homogenous oceanic crust compared to the thicker and more heterogeneous continental crust. Typically, fundamental-mode Rayleigh waves extracted from the primary microseism band (12–30 s) are used to image the oceanic crust and upper mantle. Ocean-bottom data also often display clear overtone Rayleigh-wave energy in the secondary microseism band (3–12 s) that can be used to probe the crust and uppermost mantle in extraordinary detail (Bowden *et al.*, 2016; Yang *et al.*, 2020; Russell *et al.*, 2022), unlike typical continental settings, which often exhibit complex

scattering and directional noise sources and, thus, lower signal-to-noise ratios (SNRs) in this band.

However, the ocean also poses unique challenges. Because BBOBS are deployed at the boundary between the ocean and solid Earth, interface waves primarily sensitive to the water column and shallow sedimentary layers are commonly observed in interstation noise cross-correlation functions (CCFs) at short periods (Fig. 1a). These are high-amplitude phases that travel at or below the sound speed of water (~1.5 km/s) are visible on vertical (Z), pressure (P), and radial (R) components (Fig. S1, available in the supplemental material to this article), and may be the most prominent arrivals before mitigation (Harmon *et al.*, 2007; Yao *et al.*, 2011; Takeo *et al.*, 2014; Yeck *et al.*, 2017). They are fundamental-mode interface waves trapped at the seafloor interface (Ruan *et al.*, 2014) and are typically observed only at periods <~10 s. Interface waves at

1. Department of Earth Sciences, University of Hawai'i at Mānoa, Honolulu, Hawaii, U.S.A.,  <https://orcid.org/0000-0003-1425-7969> (H AJ); 2. Department of Earth and Environmental Sciences, Syracuse University, Syracuse, New York, U.S.A.,  <https://orcid.org/0000-0003-3251-2919> (JBR)

*Corresponding author: hajanisz@hawaii.edu

© Seismological Society of America

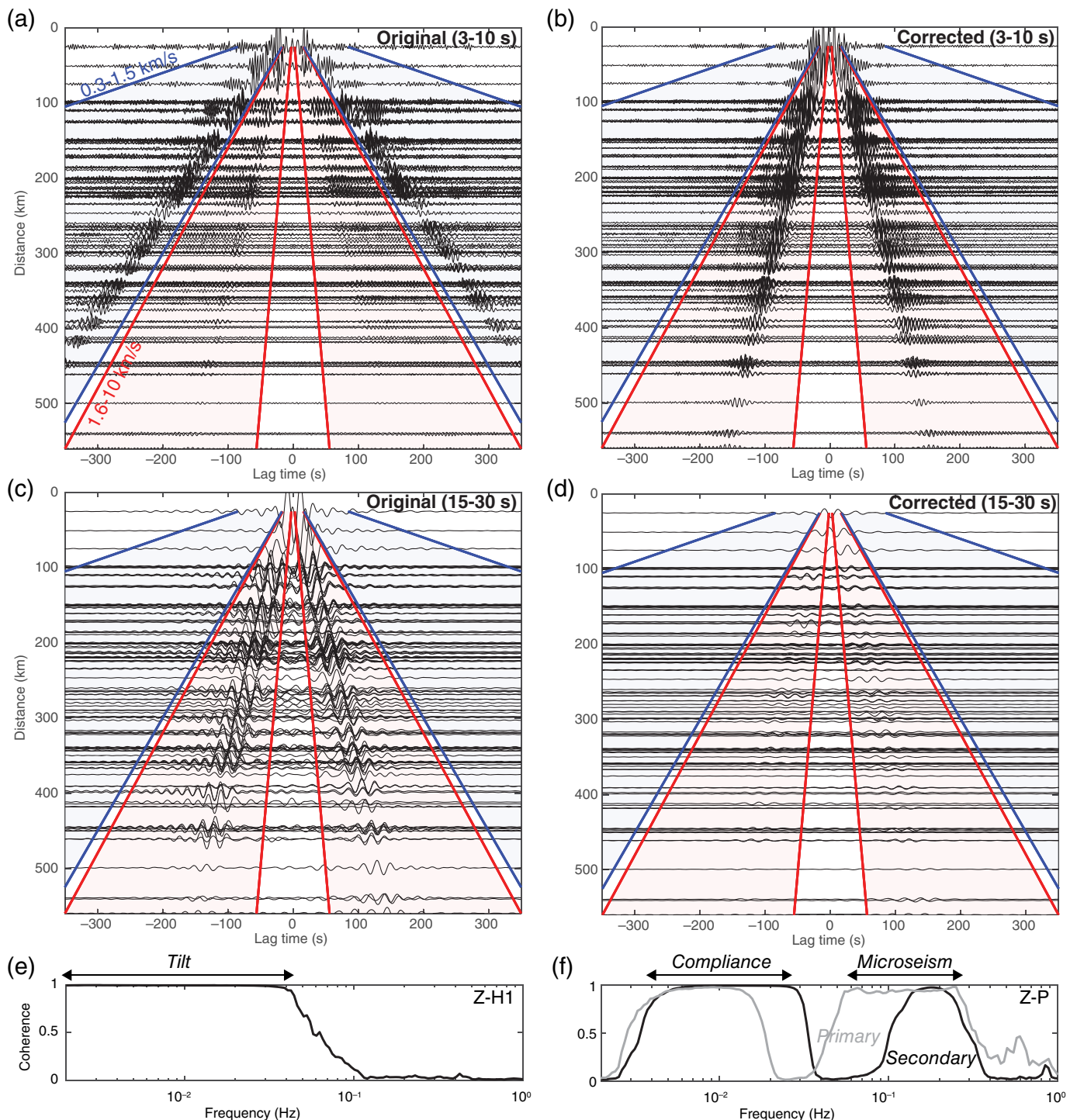


Figure 1. Example of ambient noise Z-Z cross-correlation functions (CCFs) from the NoMelt deployment filtered between 3 and 10 s (a) before and (b) after transfer function (TF) corrections, and filtered between 15 and 30 s (c) before and (d) after TF corrections. The same amplitude normalization factor is used in all panels, so amplitudes can be directly compared. Red and blue regions indicate the 1.6–10 and 0.3–1.5 km/s group velocity windows, which represent the solid- and water-velocity windows, respectively. (e) Coherence between Z and H1

components on station YO.X02, which exhibits strong tilt noise indicated by the high coherence at frequencies <0.1 Hz. (f) Coherence between Z and P components on stations 7D.M07A (black) and 2D.OBS07 (gray). At lower frequencies high coherence indicates strong compliance noise. High coherence at shorter periods is due to the microseism, which may be focused either within the secondary frequency band, or may span across the primary and secondary bands. The color version of this figure is available only in the electronic edition.

this solid–fluid boundary consist of a combination of Scholte waves and leaky Rayleigh waves (Scholte, 1947; Zhu and Popovics, 2006), both of which have elliptical particle motion similar to Rayleigh waves but with displacements highly focused at this interface. They are distinguished from one another by their predominant sensitivity to either sediments or the water column (Zhu and Popovics, 2006). Seismic ambient noise tomography literature uses a variety of terminology to refer to these waves, including Rayleigh waves, Scholte waves, or Rayleigh–Scholte waves (Nolet and Dorman, 1996; Ruan et al., 2014; Le et al., 2017; Adimah and Padhy, 2019; Hable et al., 2019; Williams et al., 2019). Herein, for simplicity we refer to these collectively as “fundamental-mode Scholte waves,” because the distinction between these waves depends on the shallow subsurface structure, which is often poorly constrained.

Short-period CCFs (~ 10 s) can also contain overtones sensitive to solid–earth structure. In contrast to the fundamental-mode Scholte waves, overtones are observed only on the Z-Z and R-R CCFs, and are characterized by faster velocities (Harmon et al., 2007; Fig. S1). Typically, the first overtone is the most prominent, and we refer to these as “first-overtone Rayleigh waves.” At longer periods ($> \sim 15$ s), fundamental-mode Rayleigh waves predominantly sensitive to solid–earth mantle structure dominate the Z-Z CCFs (Fig. 1c). Studies may use these longer periods to avoid the complications of multiple modes at shorter periods (Janiszewski et al., 2019; Doran and Laske, 2020; Pinzón et al., 2023). Although technically these are also fluid–solid interface waves, their sensitivity to the water column and sediment is negligible. Thus, here we refer to them as “fundamental-mode Rayleigh waves.”

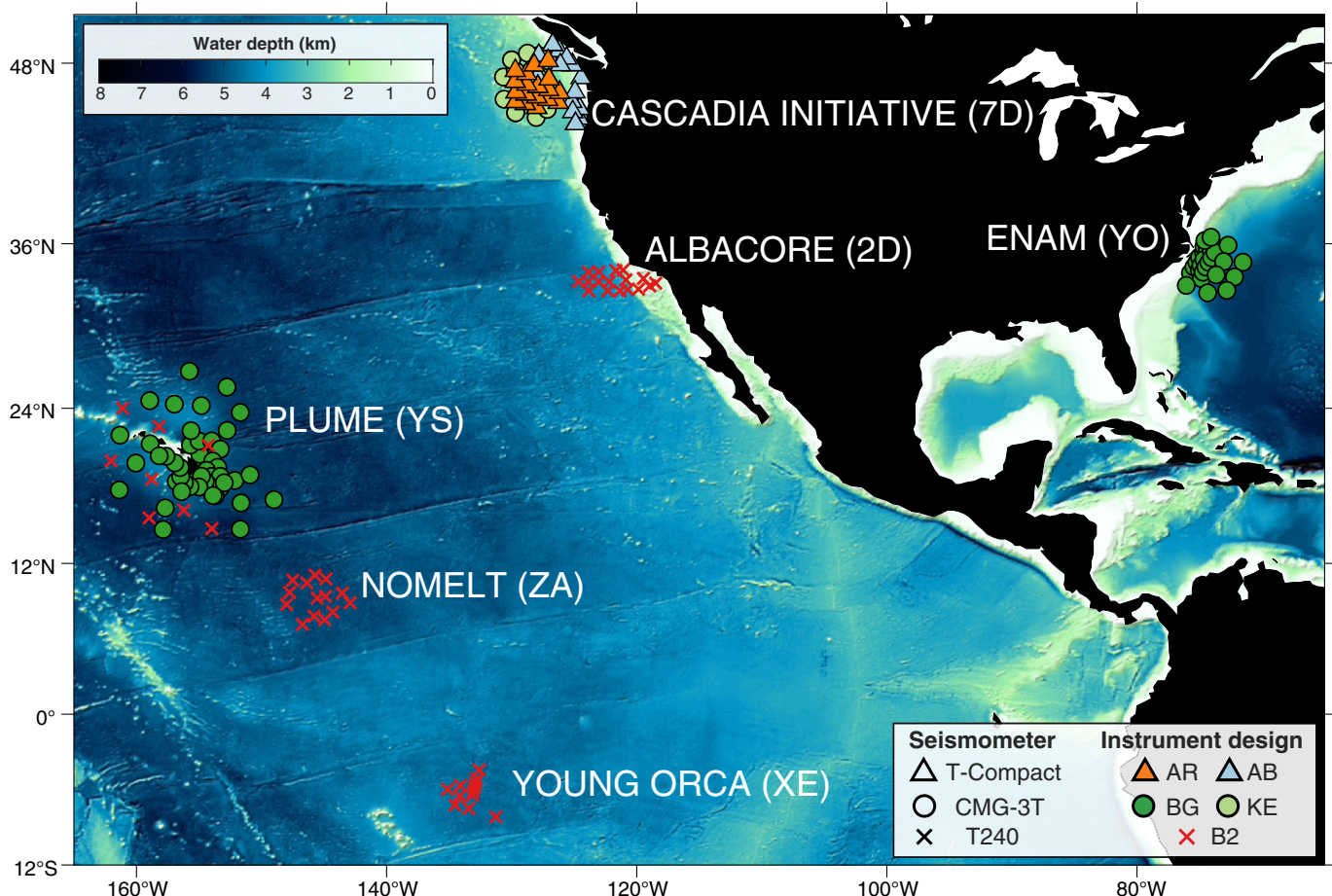
Oceanographic noise can also degrade ambient noise CCFs (Tian and Ritzwoller, 2017). On the Z component, two predominant noise sources are tilt and compliance (Crawford and Webb, 2000). The former is due to bottom currents acting on a tilted Z component, identified via spectral coherence between Z and horizontal (H1, H2) components (Fig. 1e), and is typically observed at periods > 10 s (Webb, 1998). The latter is due to infragravity waves displacing the seafloor and is identified via spectral coherence between Z and P components (Fig. 1f). Its period range depends on water depth; at a depth of 5000 m compliance noise is only present at periods $> \sim 56$ s, whereas at a depth of 100 m it exists at periods $> \sim 8$ s (Crawford et al., 1991; Webb and Crawford, 2010).

Both tilt and compliance noise can be reduced on the Z component via transfer function (TF) corrections (Crawford and Webb, 2000; Bell et al., 2015; Janiszewski et al., 2019). These are traditionally only applied at periods longer than the limits for each respective noise source and can improve the quality of Z-component ambient noise CCFs (Tian and Ritzwoller, 2017; Russell and Gaherty, 2021). High spectral coherences between the Z and P components of BBOBS are also routinely observed between ~ 3 and 10 s period in the secondary microseism band

(Janiszewski et al., 2023; Fig. 1f). P-Z TF corrections applied to 3–10 s ambient noise CCFs reduce or remove the fundamental Scholte wave (Fig. 1b) and either preserve or amplify the first-overtone Rayleigh wave (Bowden et al., 2016; Adimah et al., 2024). This is because the fundamental Scholte wave is well recorded on both the Z- and P-component CCFs in this period band, whereas the first-overtone Rayleigh wave is only recorded on the Z component (Yang et al., 2020; Kawano et al., 2023; Fig. S1). We note that high spectral coherence due to the microseism can sometimes extend to longer periods (Fig. 1f), although precisely what causes this variability remains unclear (Janiszewski et al., 2023). To distinguish from the infragravity-induced compliance correction, we refer to TF corrections between P and Z components in the microseism band as the “microseism correction” in our discussion (Ruan et al., 2014).

A variety of BBOBS ambient noise studies have characterized observations of the fundamental-mode Scholte wave, first-overtone or fundamental-mode Rayleigh wave, and the effects of TF corrections in coastal and open-ocean environments in the Pacific, Atlantic, and Indian Oceans (Harmon et al., 2007; Yao et al., 2011; Takeo et al., 2014; Bowden et al., 2016; Takeo et al., 2016; Yeck et al., 2017; Adimah and Padhy, 2019; Hable et al., 2019; Yang et al., 2020; Wolf et al., 2021; Kawano et al., 2023; Pinzón et al., 2023). Unfortunately, these studies often use different preprocessing and noise-mitigation strategies, precluding direct comparisons. They also focus on individual BBOBS deployments, which typically have similar noise characteristics due to their limited environmental and instrumental variability (Janiszewski et al., 2023).

Here, we use data from a subset of recent U.S.-led BBOBS deployments to compare self-consistently calculated ambient noise CCFs both pre- and post-noise mitigation via TFs. We focus on the 3–10 and 15–30 s period bands, which are commonly used for crustal and upper-mantle tomography, respectively. These bands typically exhibit phase- and group-velocity curves that are relatively flat, resulting in comparatively simple CCFs. In contrast, the 10–15 s band spans the transition between Scholte and Rayleigh waves and is characterized by a steep phase- and group-velocity gradient, which complicates the resulting CCFs. In addition, microseism noise amplitudes peak within these bands, typically yielding high-quality CCFs (McNamara and Buland, 2004; Bensen et al., 2007). Although ambient noise tomography at periods shorter than 3 s or longer than 30 s is possible, these analyses at modern BBOBS arrays can be limited by array density or aperture, respectively. Within our selected period bands, we compare the results systematically across deployments and assess the features and quality of the CCFs in the context of environment, instrumentation, and noise properties. This provides new insights into the key variables affecting data quality, and practical guidance for improving future BBOBS ambient noise tomography. Such observations are relevant not only for traditional BBOBS arrays but also for emerging methodologies such as dense ocean-bottom nodal



deployments, distributed acoustic sensing (DAS), and long-term cabled seafloor instrumentation.

Data and Methods

Deployments and instrumentation

We examine data from six BBOBS deployments (Fig. 2): (1) PLUME (Wolfe *et al.*, 2009); (2) ALBACORE (Lin *et al.*, 2015); (3) the Juan de Fuca portion of Cascadia Initiative (Toomey *et al.*, 2014); (4) NoMelt (Lin *et al.*, 2016); (5) ENAM (Lynner *et al.*, 2019); and (6) Young ORCA (Eilon *et al.*, 2021). Each was deployed with instrumentation from the Ocean-Bottom Seismic Instrument Pool (OBSIP) or Ocean-Bottom Seismic Instrument Center (OBSIC) between 2005 and 2020 (Aderhold *et al.*, 2019). Detailed site and instrument metadata are assembled by Janiszewski *et al.* (2023). For each deployment, BBOBS are equipped with a three-component broadband seismometer and a pressure gauge yielding a total of four individual components per instrument. The dataset contains 193 BBOBS, although not all instruments have four operational components.

These BBOBS sample a variety of parameters that are known to affect noise in our period bands of interest. Janiszewski *et al.* (2023) find that water depth, seismometer type, and instrument design play significant roles regulating tilt and compliance noise properties. Our included BBOBS are deployed at water depths

Figure 2. Map of stations analyzed and their corresponding deployments with names and network codes. Symbols and colors indicate seismometer type and instrument design as detailed in Table 1. The color version of this figure is available only in the electronic edition.

between ~50 and 6000 m. Each uses one of three types of seismometers: Guralp CMG-3T (CMG-3T), Nanometrics Trillium Compact (T-Compact), and Nanometrics Trillium 240 (T-240). All instruments also include a differential pressure gauge (DPG). Our dataset incorporates five distinct instrument designs (Table 1).

Similarly, primary and secondary microseism noise sources are impacted by water depth, ocean basin characteristics, and subsurface structure, although less is known about how this impacts their viability for imaging. The primary microseism is caused by the interaction of waves with small-scale seafloor topography at shallow water depth, and large-scale slopes near coastlines (Ardhuin *et al.*, 2015). On the shallow continental shelf, the primary microseism is amplified relative to the open ocean, and relative to the secondary microseism (Webb and Crawford, 2010). The secondary microseism is caused by interacting waves either from oblique intersection, coastline reflection, or storm-generated swell interactions (Ardhuin *et al.*,

TABLE 1
Instrument Design Details

Abbreviation	Design Institution	Seismometer	Pressure Gauge	Instrument Name
AB	SIO	T-Compact	DPG	Abalone
B2	SIO	T-240	DPG	SIO unshielded broadband
AR	WHOI	T-Compact	DPG	WHOI ARRA
BG	WHOI	CMG-3T	DPG	WHOI BBOBS
KE	WHOI	CMG-3T	DPG	WHOI KECK

ARRA and KECK refer to instruments on the OBSIC website; BBOBS, broadband ocean-bottom seismometer; DPG, differential pressure gauge; SIO, Scripps Institution for Oceanography; WHOI, Woods Hole Oceanographic Institution.

2011). Systematic differences in the amplitude and frequency range of the secondary microseism power spectral density (PSD) peak are observed between the Pacific and Atlantic basins (Babcock *et al.*, 1994). Furthermore, Ruan *et al.* (2014) show that sedimentary thickness and velocity structure also impact seismometer response in the secondary microseism band. To investigate these factors, our dataset includes BBOBS in both coastal and open-ocean environments, in the Pacific and Atlantic Oceans, and with sedimentary thicknesses from ~0 to 8000 m.

Unfortunately, we cannot completely isolate these variables with existing BBOBS datasets (Janiszewski *et al.*, 2023). For example, shallow coastal regions often are heavily sedimented and require shielded BBOBS designs. However, to our knowledge this represents the most comprehensive assembled dataset for systematic analysis of the quality of ambient noise CCFs observed on BBOBS to date.

TFs

The TF describes the linear relationship between common signals present on any two components of a BBOBS, which can be used to identify and remove coherent noise (Crawford and Webb, 2000). This is particularly valuable because it does not require a full understanding of the noise source—only that the noise appears coherently across components. Here, we summarize the TF theory and terminology relevant to this study.

We define the cross spectrum between two components $x(t)$ and $z(t)$ as: $G_{ZX}(f) = Z^*(f)X(f)$, in which $Z(f)$ is the Fourier transform of $z(t)$ and $Z^*(f)$ is its complex conjugate. Similarly, the power spectrum of $x(t)$ is defined as: $G_{XX}(f) = X^*(f)X(f)$. Using the cross spectrum of any two components and the power spectrum of the reference component, a TF can be calculated that describes the linear mapping of signals common to both components. Treating Z as the component of interest we want to correct, and X as the component containing noise, we define the TF T_{ZX} as

$$T_{ZX}(f) = \frac{G_{ZX}(f)}{G_{XX}(f)}. \quad (1)$$

This TF can then be used to correct the Z component for the common noise present on the X component in the frequency domain:

$$Z_{\text{corr}}(f) = Z(f) - T_{ZX}^*(f)X(f). \quad (2)$$

Ambient noise CCFs

Z -component ambient noise CCFs are calculated following the procedure of Russell and Gaherty (2021). We divide daily displacement seismograms into 15 three-hour windows with 50% overlap. The cross-spectral coherence $\rho_{ij}(f)$ between two stations i and j is calculated in the frequency domain for each time window k and summed over all N windows of the deployment:

$$\rho_{ij}(f) = \frac{1}{N} \sum_{k=1}^N \frac{Z_{ik}^*(f) \times Z_{jk}(f)}{|Z_{ik}(f)| \times |Z_{jk}(f)|}, \quad (3)$$

in which $Z(f)$ is the vertical displacement spectrum at frequency f , and $Z^*(f)$ is its complex conjugate. This definition of the CCF results in spectral whitening, and we do not apply additional time-domain normalization or other spectral conditioning. By stacking many short-time windows, transient signals such as earthquakes do not need to be removed as any individual windows containing such signals have a small influence on the overall CCF stack.

We remove coherent H1, H2, and P energy from the daily Z records using the TF approach as implemented by automated tilt and compliance removal (ATaCR) package (Janiszewski *et al.*, 2019). We use a modified code that does not include quality control steps for removing anomalous TFs (see Data and Resources). We calculate mean daily spectra from 24-hr seismograms by dividing each day into 20 windows of length 6000 s with ~50% overlap. Mean H1-Z, H2-Z, and P-Z TFs are then calculated for each 24-hr segment of data. For each record, H1-Z and H2-Z TF corrections are applied first to target the tilt correction, followed by P-Z TF corrections to target the compliance and microseism corrections across all periods. Using these corrected seismograms, we recalculate the CCFs using equation (3). These corrected CCFs show

noticeable changes in the amplitude of the fundamental-mode Scholte, first-overtone Rayleigh, and fundamental-mode Rayleigh waves (Fig. 1, Fig. S2).

To quantify differences between the original and corrected CCFs, we define metrics for the change in SNR of expected interface wave arrivals for the two period bands of interest. In the 3–10 s period band, we calculate SNR in two group velocity windows: 1.6–10 km/s to target the faster first-overtone Rayleigh wave, and 0.3–1.5 km/s to target the slower fundamental-mode Scholte wave. We term the faster and slower velocity windows as the “solid-velocity” and “water-velocity” window, respectively. In the 15–30 s period band, we isolate the expected fundamental Rayleigh wave using a group velocity window of 1.6–10 km/s. We ignore the water-velocity window because we do not expect to observe a Scholte wave in this band (Nolet and Dorman, 1996). In each case, the windowed portion of the seismogram is considered the signal u_s and SNR is calculated as

$$\text{SNR} = \frac{N_s^{-1} \sum_{s=1}^{N_s} u_s^2}{N_n^{-1} \sum_{n=1}^{N_n} u_n^2}, \quad (4)$$

in which u_n is the noise defined between 4000 and 5000 s lag time. Finally, for each period band and group velocity window, we calculate the change in SNR between the original and TF corrected CCFs as

$$\Delta\text{SNR} = \log_{10} \frac{\text{SNR}_{\text{corr}}}{\text{SNR}_{\text{orig}}}, \quad (5)$$

in which positive values indicate SNR improvement after correction and negative values indicate SNR decline.

Noise spectral properties

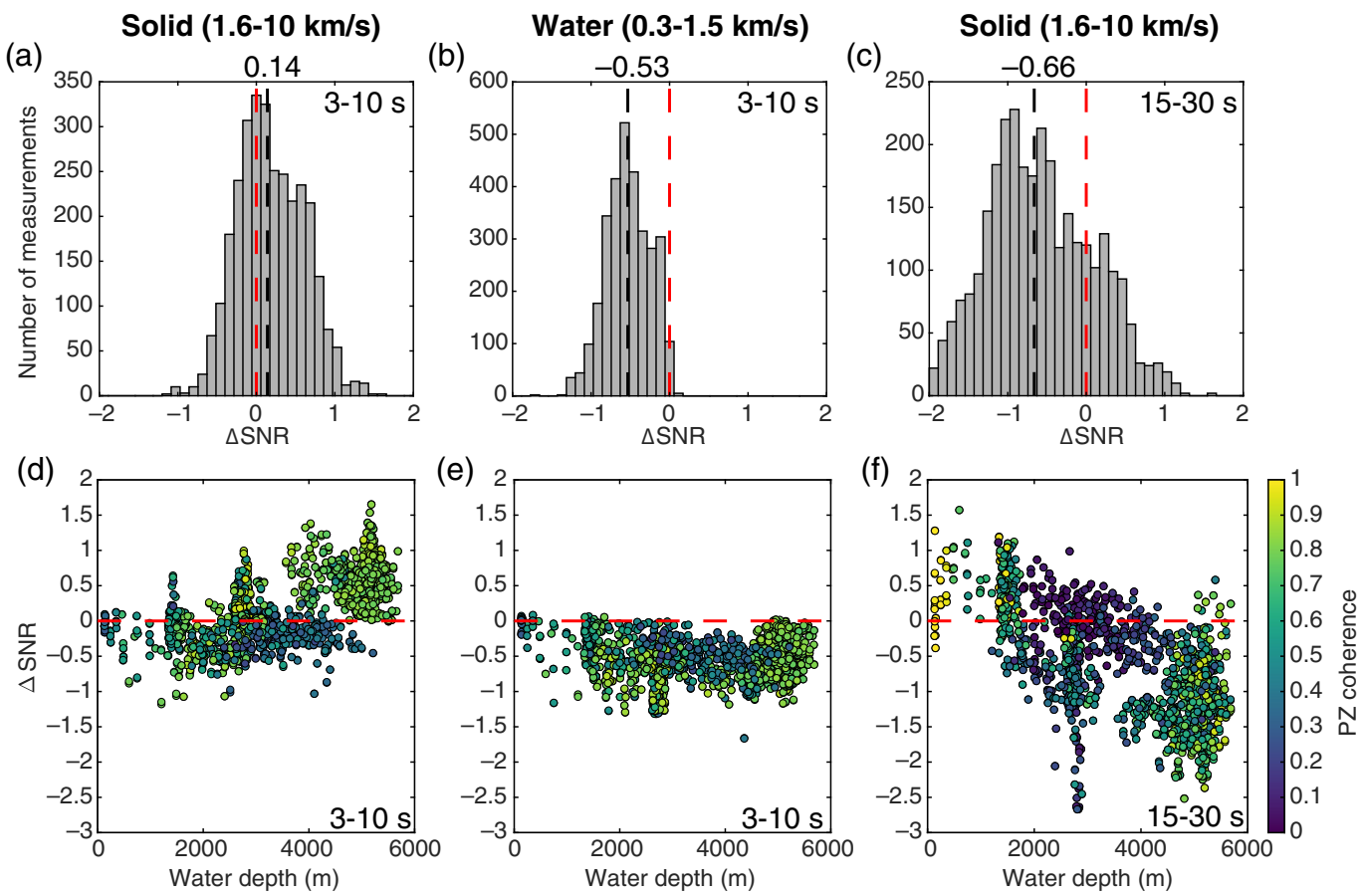
To understand causes of variability in the CCF SNRs and the effect of TF corrections, we examine these results in the context of spectral properties for each BBOBS. We use the PSD and cross-component admittance, coherence, and phase for each station from Janiszewski *et al.* (2023); details of the methodology are given therein. Components with data dropouts, glitches, or other anomalies are discarded. We require that BBOBS have four operational components, producing a total of 155 instruments used for subsequent analyses. In particular, we use spectral coherence as a metric to compare with the ΔSNR of the CCFs. Because coherence ranges from 0 to 1, it facilitates comparisons across instruments as it is indifferent to gain or polarity. Generally, where coherence is low, TF removal has little effect and vice versa; thus, we expect to observe a strong relationship between coherence and ΔSNR . We octave-average the coherence function in 1/16 intervals following McNamara and Buland (2004) and then calculate mean coherence in the 15–30 and 3–10 s period bands. Here, we use PZ coherence to refer to the coherences after tilt noise has already been removed.

Results

After we apply H1-Z, H2-Z, and P-Z TF corrections in the 3–10 s band, the mean ΔSNR is positive in the solid-velocity window, and negative in the water-velocity window (Fig. 3a,b). This is consistent with the expected behavior for the first-overtone Rayleigh wave and the fundamental-mode Scholte wave. Although the mean improvement of the first-overtone Rayleigh-wave signal is small, ~63% of the CCFs are improved, in some cases exceeding a factor of 10 increases in SNR. However, the remainder of CCFs shows a decrease in SNR after correction in this window, indicating that TF corrections in some instances reduce data quality. By contrast, nearly all measurements (~99%) of the fundamental-mode Scholte wave have a reduced SNR, indicating that the TFs reliably remove this wave from CCFs. After only horizontal TFs, ΔSNR changes minimally in both velocity windows (Fig. S3a,b), consistent with the minimal tilt noise expected in this band. After applying the H1-Z, H2-Z, and P-Z TF corrections in the 15–30 s band, the mean ΔSNR is negative; however, ~22% of the CCFs improve (Fig. 3c). Thus, the correction reduces the fundamental-mode Rayleigh-wave SNR for the majority of the CCFs. The horizontal correction alone results in no change in the mean ΔSNR ; however, at some stations ΔSNR increases (Fig. S3c), which is expected if the TF correction successfully removes tilt noise. This is consistent with the previous observation that tilt noise only dominates on a subset of instrument types (Bell *et al.*, 2015; Janiszewski *et al.*, 2023).

Although the mean behavior of ΔSNR aligns with expectations, there is significant variability in the effect of corrections, particularly for the Rayleigh waves. To investigate the cause of this variability, we calculate covariance between the following: SNR of the original CCFs, ΔSNR , PZ coherence, water depth, and interstation pair distance (Fig. 4). For the coherence and water depth, we use the mean of each station pair, and water depth is a positive value.

In the 3–10 s band, the $\Delta\text{SNR}_{\text{solid}}$ for the first-overtone Rayleigh wave is positively correlated with PZ coherence and water depth, with values of 0.45 and 0.60, respectively. This indicates that the correction is most effective for higher PZ coherences and deeper stations (Fig. 3d, Fig. S4a). In contrast, $\Delta\text{SNR}_{\text{water}}$ for the fundamental-mode Scholte wave is not highly correlated with these (Fig. 3e, Fig. S4b) but instead is negatively correlated (-0.72) with its original SNR. This indicates that a higher SNR fundamental-mode Scholte wave in the original CCF is more effectively removed via TF corrections. The $\Delta\text{SNR}_{\text{water}}$ for the fundamental-mode Scholte wave is also negatively correlated (-0.59) with the original SNR of the first-overtone Rayleigh wave; however, this is likely driven by a high-positive correlation (0.88) between the original SNRs in the solid- and water-velocity windows. Finally, the original SNR of both the fundamental-mode Scholte wave and first-overtone Rayleigh wave is negatively correlated with interstation distance (-0.69 and -0.67, respectively), likely due to



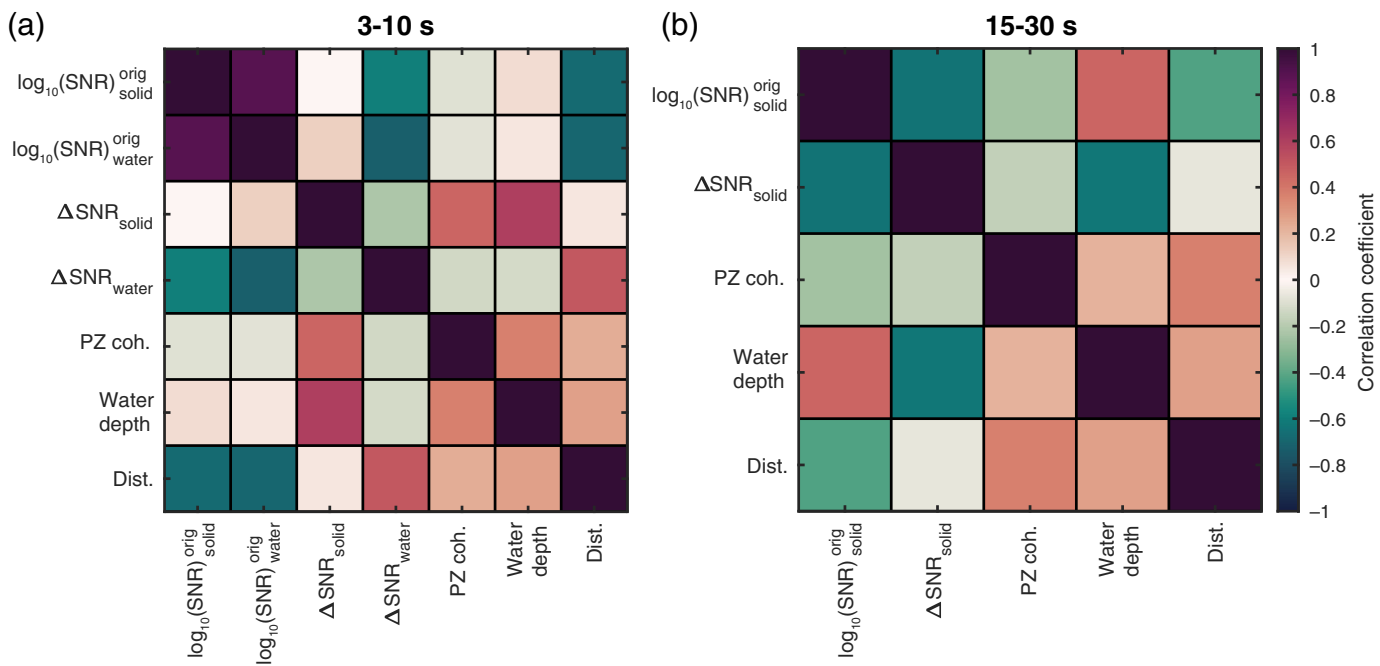
geometrical spreading and attenuation effects (Harmon et al., 2007).

In the 15–30 s band, the $\Delta\text{SNR}_{\text{solid}}$ for the fundamental-mode Rayleigh wave has a -0.62 correlation coefficient with water depth. This is opposite in direction but similar in magnitude to the correlation observed with water depth in the 3–10 s band, instead indicating that the correction is more successful in shallow water (Fig. 3f). The $\Delta\text{SNR}_{\text{solid}}$ is only weakly correlated (-0.16) with PZ coherence in the 15–30 s band (Fig. S4c), substantially weaker than the correlation in the 3–10 s band. The $\Delta\text{SNR}_{\text{solid}}$ for the fundamental-mode Rayleigh wave has a negative correlation coefficient (-0.64) with the original SNR, which indicates that the TF correction either reduces signal if the original CCF has high SNR (e.g., Fig. 1) or reduces noise if the original CCF has low SNR. Furthermore, the original SNR of the fundamental-mode Rayleigh wave has a positive correlation coefficient of 0.45 with water depth, indicating that deeper stations generally have higher original SNR values before corrections. Finally, a negative correlation of -0.42 is observed between the original SNR and interstation distance. This is weaker than the correlation observed in the 3–10 s band, consistent with lower attenuation for the same distances at longer periods.

In summary, water depth and, to a lesser extent, PZ coherence are strongly related to ΔSNR for both the first-overtone and fundamental-mode Rayleigh waves (i.e., waves within the

Figure 3. Histograms of the change in signal-to-noise ratio (ΔSNR) for the CCFs for the (a) solid-velocity window at 3–10 s, (b) water-velocity window at 3–10 s, and (c) solid-velocity window at 15–30 s. The red dashed line indicates the zero axis, or no change. The black dashed line indicates the mean ΔSNR . Here, H1-Z, H2-Z, and P-Z TFs are applied. Scatter plots of the ΔSNR for each CCF as a function of mean water depth for the panel (d) solid-velocity window at 3–10 s, (e) water-velocity window at 3–10 s, and (f) solid-velocity window at 15–30 s. Color indicates mean PZ coherence for each station pair. The color version of this figure is available only in the electronic edition.

solid-velocity window) at 3–10 and 15–30 s. It is somewhat surprising that water depth yields a higher correlation coefficient than PZ coherence in both bands because PZ coherence is directly incorporated into the TF corrections. There are several limitations to our covariance analysis. First, using the mean value of parameters for each station pair obscures relationships. For example, a pair of stations both at ~2000 m water depth has a similar mean as a station pair with 100 and 4000 m water depths, respectively. Second, we cannot investigate relationships with qualitative parameters such as instrument design, seismometer, ocean basin, or deployment. Third, the covariance analysis is ill suited for relationships for which variables are not evenly sampled across our dataset. For example, sediment thickness is highly unevenly distributed with most



stations having thicknesses <1000 m but with ENAM stations sampling thicknesses up to ~8000 m. Instead, we undertake a more targeted investigation, and discuss our observations in the context of expectations for seismic and oceanographic noise behavior.

Discussion

Effects of water depth

There are two mechanisms that are likely responsible for the relationship between water depth and the effectiveness of TF corrections on the ambient noise CCFs. First, the frequency below which infragravity waves appear, and thus where compliance noise is present, is given by the dispersion relationship:

$$f \approx \sqrt{\frac{g}{2\pi d}}, \quad (6)$$

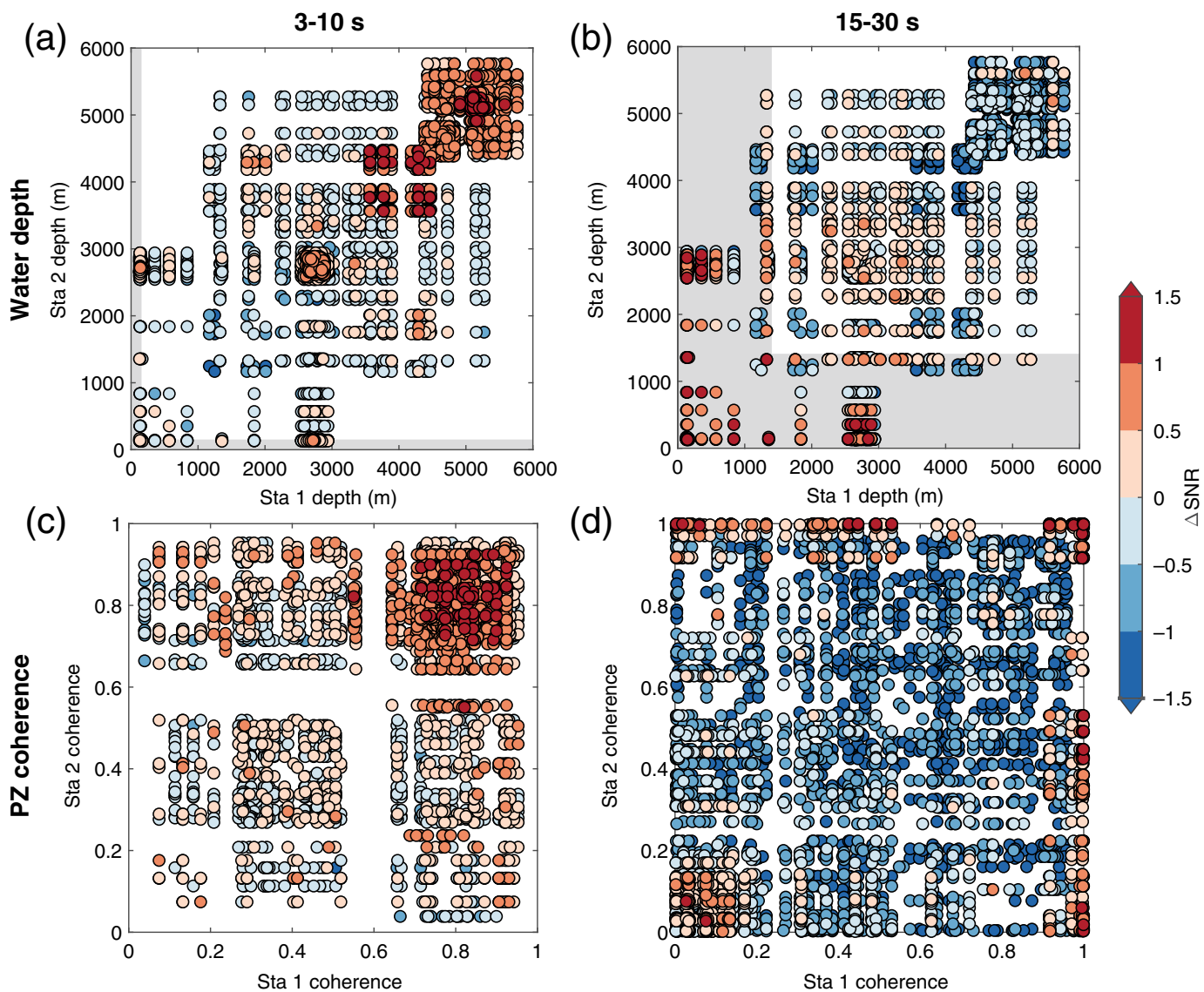
in which g is the gravity and d is the water depth (Crawford *et al.*, 1998). Because the water depth of each instrument is known, so too is this frequency. Importantly, infragravity waves result in high-PZ coherence below this cutoff frequency, particularly once tilt has been removed (Crawford and Webb, 2000). Second, variations in bathymetry, and sediment thickness and velocity impact the frequency range at which fundamental-mode Scholte waves are observed (Webb, 1992; Harmon *et al.*, 2007; Ruan *et al.*, 2014). In general, these waves extend to lower frequencies in deeper water. Increasing sediment thickness or decreasing velocity also result in their extension to lower frequencies. Because this depends on both the water depth and shallow seismic velocities beneath interstation paths, which are variably constrained for our dataset, it is difficult to predict the precise frequency transition for individual

Figure 4. Correlation coefficients for listed variables for (a) 3–10 and (b) 15–30 s periods. The color version of this figure is available only in the electronic edition.

station pairs. Here, we examine the Δ SNR for the solid-velocity window in both the 3–10 and 15–30 s period bands as compared with the water depth and PZ coherence of each member of a station pair (Fig. 5). We focus on the maximum Δ SNRs in our discussions because these provide an insight into the maximum signal improvement at a given water depth or PZ coherence.

At 3–10 s, infragravity waves only significantly affect the shallowest stations (<~150 m). For example, the shallowest station in our dataset is deployed at 126 m water depth, which corresponds to an infragravity cutoff at 9 s. Thus, much of the 3–10 s band does not record infragravity waves, even at the shallowest stations. When either member of a station pair is deployed at <150 m water depth, the maximum Δ SNR is <~0.5, indicating little to no improvements in the data after TF corrections (Fig. 5a). These correspond to relatively low-PZ coherences because the infragravity signal overlaps with only a small portion of the target period range. Because these waves arrive within the solid-velocity window, they are Rayleigh waves predominantly sensitive to solid-earth structure; however, it is unclear if they are fundamental or first-overtone phases. Although most solid-velocity arrivals are first overtones at 3–10 s, the transition between modes should shift to shorter periods in shallow water (Ruan *et al.*, 2014; Tian and Ritzwoller, 2017).

The most significant improvements of the CCFs in the solid-velocity window in the 3–10 s band occur in deeper water



($> \sim 3500$ m), and where both stations in a pair have similar water depths ($< \sim 1000$ m difference). These pairs typically have high-PZ coherence ($> \sim 0.7$), which is due to the secondary microseism and not the infragravity signal (Fig. 5c). Corrections applied under these conditions yield $\Delta\text{SNR} > 1$ (Fig. 5a), reflecting enhanced detection of the first-overtone Rayleigh mode. In contrast, station pairs with shallower depths or large depth differences tend to have smaller or negative ΔSNR values, despite varying levels of PZ coherence. This indicates that high coherence alone is not sufficient for successful correction (Fig. S4a). Although there is a general positive correlation between ΔSNR and mean water depth or PZ coherence, these results emphasize that both absolute depth and interstation depth differences are critical for improving first-overtone Rayleigh-wave signals after TF corrections. Notably, some deployments deviate from this trend: ENAM stations consistently show lower ΔSNR values, even for water depths > 3500 m and station pair depth differences < 1000 m (Fig. S5).

Figure 5. Scatter plots showing ΔSNR in the solid-velocity window as a function of (a,b) the water depth and (c,d) the PZ coherence of each member of a station pair for (a,c) 3–10 and (b,d) 15–30 s period bands. For water depth, gray shading indicates depth range overlapping with the infragravity band at (a) 10 and (b) 30 s. Note that individual points overlap; points with the highest ΔSNR values are plotted on top. The color version of this figure is available only in the electronic edition.

We observe markedly different behaviors at 15–30 s. At 30 s period, the infragravity wave is observable on stations at water depths $< \sim 1400$ m. For station pairs with at least one station in this depth range, the corrections effectively remove infragravity wave noise, resulting in the greatest signal improvements of $\Delta\text{SNR} > 1$ (Fig. 5b). This is likely the primary improvement previously observed at the Cascadia Initiative experiment by Tian and Ritzwoller (2017). These predominantly correspond to station pairs where PZ coherence is very high ($> \sim 0.95$) on

at least one station, although we note that the accompanying station may have coherences as low as ~ 0 (Fig. 5d). In contrast, most station pairs deployed at depths >1400 m show reduced signal quality ($\Delta\text{SNR} < 0$). This is consistent with the negative correlation coefficient between ΔSNR and mean water depth (Fig. 4b), supporting the dominant role of infragravity wave removal at these periods. In addition, station pairs at water depths >1400 m have $\Delta\text{SNR} < 0$ even when PZ coherence is high (Fig. 5d, Fig. S5). High-PZ coherences at these water depths cannot arise from infragravity waves, and instead are driven by the presence of primary microseism-generated Rayleigh waves (e.g., Fig. 1f). The resulting negative ΔSNRs indicate that the TF corrections remove part of the desired fundamental-mode Rayleigh-wave signal.

We also observe moderate improvements ($0 < \Delta\text{SNR} < 1$) at some stations with water depths >1400 m, most of which correspond to low-PZ coherences (<0.2) on both stations (Fig. 5d). This bimodal relationship between PZ coherence and ΔSNR is markedly different than observations in the 3–10 s band (Fig. 5c), and the cause of this variability is not explained by infragravity waves. Only three deployments—ENAM, Cascadia Initiative, and PLUME—contain instruments with positive ΔSNRs at >1400 m water depth, and the majority of high ΔSNRs (>0.5) that are accompanied by low-PZ coherence are restricted to ENAM (Fig. S5). Overall, these results highlight the complex interplay between water depth, noise sources, and the success of TF corrections, emphasizing the importance of considering both station depth and pair configuration when deciding how to analyze CCFs.

Effects of tilt noise

We posit that positive ΔSNRs at water depths >1400 m in the 15–30 s period band are instead driven by the correction of tilt noise on the CCFs. Previous analyses of BBOBS noise properties demonstrate that tilt noise is highly dependent on the seismometer and instrument design (Bell *et al.*, 2015; Janiszewski *et al.*, 2023). To investigate the influence of tilt noise on the CCFs, we examine the difference between the mean PZ coherence and HZ coherence for each station pair (Fig. 6). We define the HZ coherence as the maximum of the H1-Z and H2-Z coherences. When tilt noise is present and stronger than compliance noise, the HZ coherence should be high (Crawford and Webb, 2000). Because we do not rotate the horizontals into the maximum tilt direction, the HZ coherence should not necessarily equal one at a high tilt station. However, in the absence of tilt noise, the H1-Z and H2-Z coherences should both be close to zero (Bell *et al.*, 2015); thus, a nonzero HZ coherence should serve as a reasonable diagnostic for tilt noise. After tilt noise is removed, the PZ coherence increases substantially within the infragravity band due to compliance noise (Bell *et al.*, 2015). The PZ coherence due to the microseism may also moderately increase if its frequency range overlaps with the tilt noise (Janiszewski *et al.*, 2023). We can distinguish between

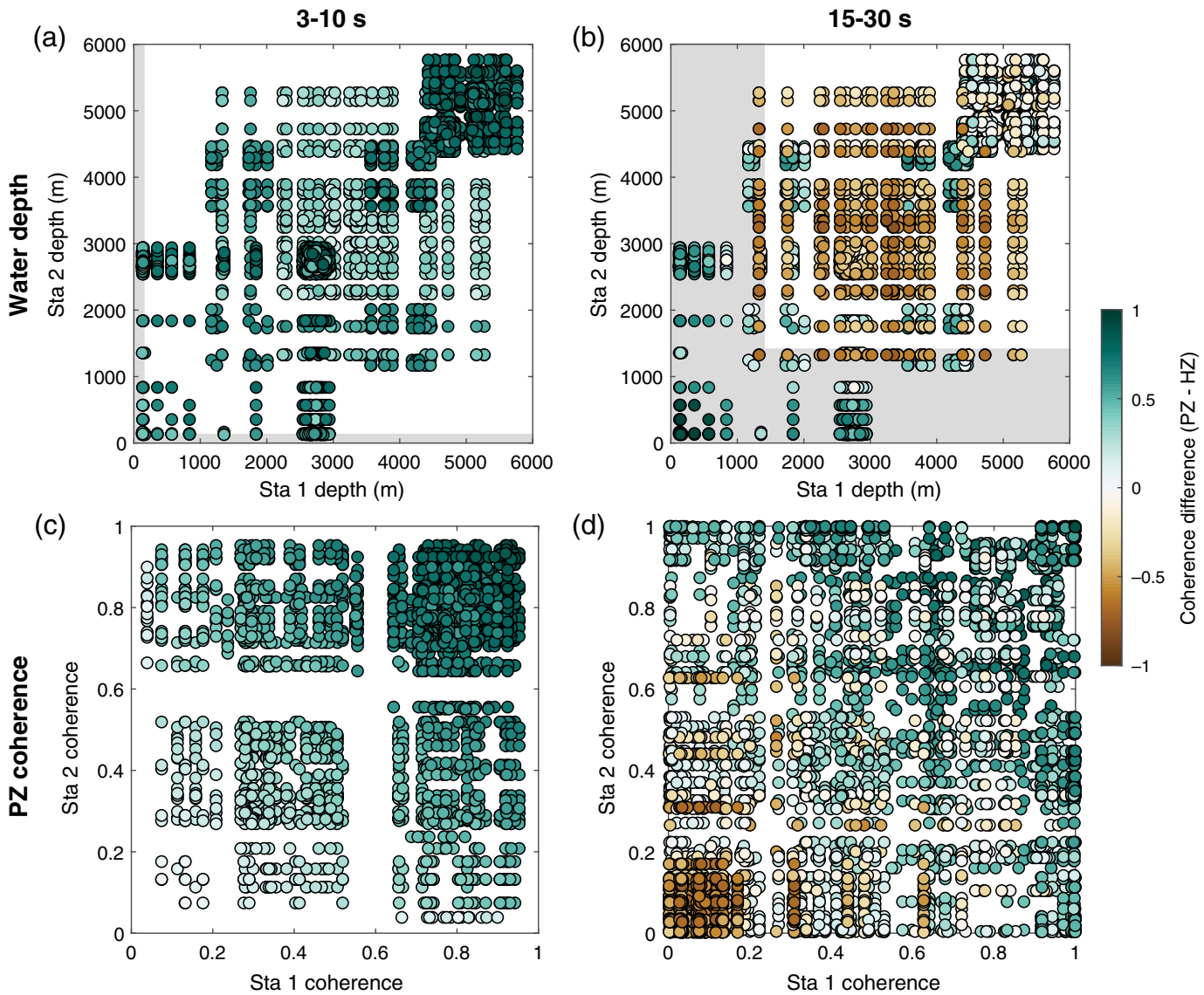
high-PZ coherence due to the infragravity wave versus the microseism using the water-depth cutoff-frequency relationship in equation (6).

By differencing the PZ and HZ coherence, we examine the relative strength of tilt, compliance, and coherent microseism noise. Negative values indicate higher HZ coherence (stronger tilt noise), whereas positive values indicate higher PZ coherence (stronger compliance or coherent microseism noise). Near-zero values indicate either similar magnitudes of HZ and PZ coherences (comparable tilt, and compliance or microseism noise) or an absence of any coherence. We discriminate between these possibilities by comparing PZ-HZ coherence with PZ coherence (Fig. 6c,d). The subset of stations with low-PZ coherence but high ΔSNR in the 15–30 s band (Fig. 5d) corresponds to the most negative PZ-HZ coherence values (Fig. 6d). Because these station-pair water depths are >1400 m, this indicates they have high tilt noise accompanied by a lack of PZ microseism coherence. Thus, the increase in ΔSNR is driven primarily by the removal of tilt noise from the CCFs. In contrast, at <1400 m water depth positive ΔSNRs accompany positive PZ-HZ coherences due to the removal of strong compliance noise.

Negative PZ-HZ values occur only at deployments with instrument designs that use CMG-3T seismometers (i.e., ENAM, Cascadia Initiative, and PLUME; Fig. S6), which have been shown to have systematically higher tilt noise than other seismometer types and instrument designs before TF corrections (Bell *et al.*, 2015; Janiszewski *et al.*, 2023). Among these deployments, ENAM shows the most negative PZ-HZ values, which are accompanied by high ΔSNRs for stations with >1400 m water depth (Figs. S5, S6). This indicates that ENAM uniquely experiences high tilt noise accompanied by lower PZ coherence in the primary microseism band. Thus, the high ΔSNRs observed at the ENAM deployment arise not only from tilt noise removal but also from a lack of removal of the fundamental-mode Rayleigh wave due to low-PZ microseism coherence. Improvement of CCFs due to tilt removal at ENAM was previously demonstrated by Russell and Gaherty (2021), and they interpreted the remarkably high tilt noise as a result of the strong Gulf Stream current. At the Cascadia Initiative and PLUME deployments, PZ microseism coherence is higher and therefore potential improvements in signal quality due to tilt noise removal are reduced due to degradation of the fundamental-mode Rayleigh wave. Here, tilt noise removal alone may yield higher ΔSNRs . Negative PZ-HZ coherences do not occur in the 3–10 s band. This is consistent with the expectation that tilt noise is absent at periods <10 s (Crawford and Webb, 2000). Instead, the PZ-HZ metric is almost entirely driven by the PZ coherence (Fig. 6c).

Impact of sediments and other factors

Although water depth has a primary control on the ΔSNR of the first-overtone Rayleigh wave in the 3–10 s band, sediment

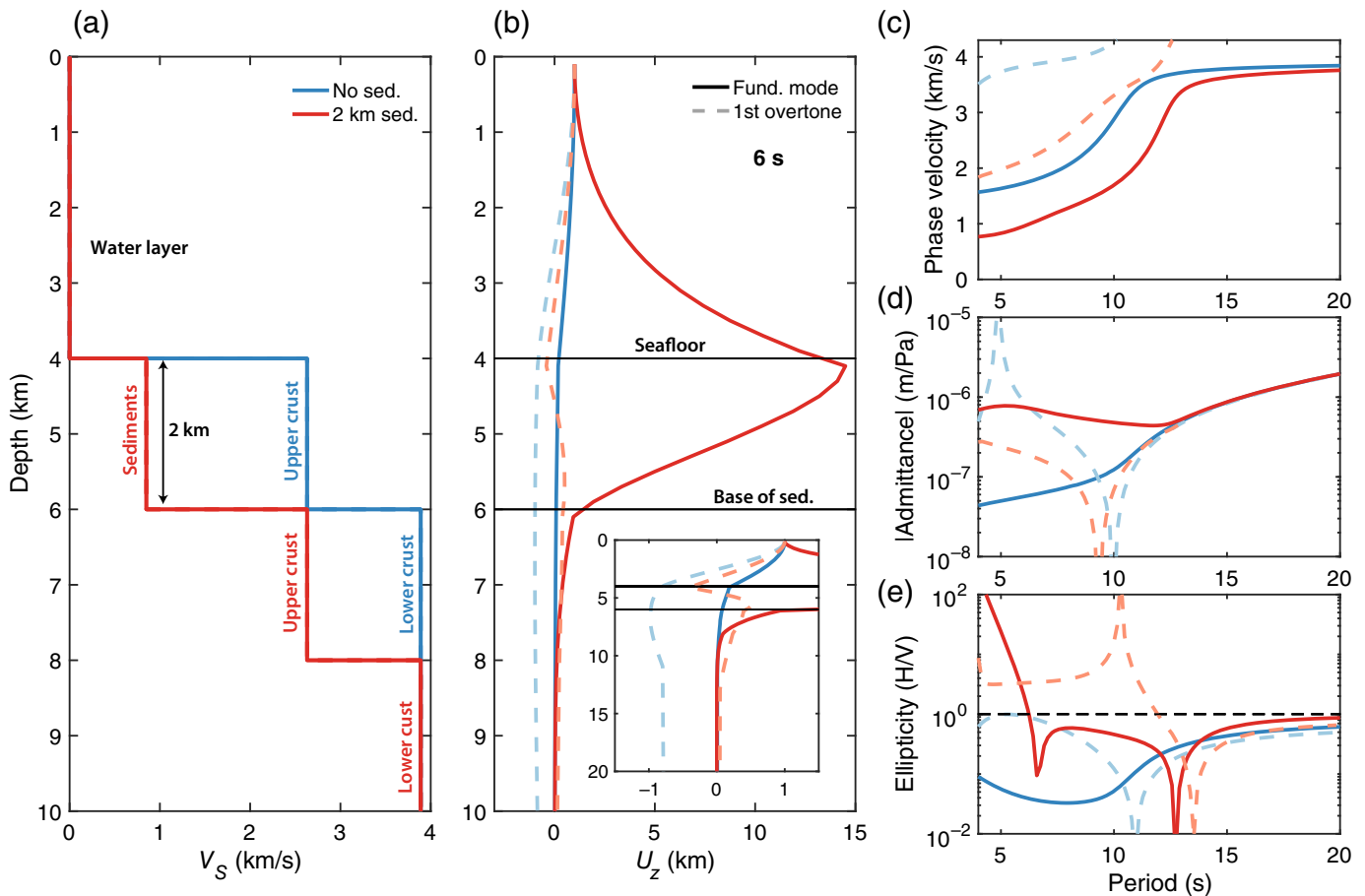


structure should also play a role (Nolet and Dorman, 1996; Zhu and Popovics, 2006; Ruan *et al.*, 2014). These two factors are often interrelated—thicker sediments are typically found on continental shelves at shallower water depths, whereas thinner layers are more common in deeper ocean basins (Straume *et al.*, 2019). ENAM is the only deployment in our analysis with sediment thickness >2000 m, reaching ~8000 m beneath some stations. It is also the only deployment with relatively deep stations (>3000 m), where the TF correction produces maximum ΔSNR s < 0 for the first-overtone Rayleigh wave. Thus, it is possible that these anomalous observations on the ENAM deployment are driven by thick sedimentary layers.

To understand the role of sediments, we explore the theoretical behavior of interface waves for two layered models: one with sediments and one without (Fig. 7a). The sediment-free model contains a 4 km thick water layer, underlain by oceanic crust (divided into a 2 km thick upper crust and 5 km thick lower crust) and mantle using velocities based on Ruan *et al.* (2014). The second model is identical to the first, but includes a

Figure 6. Scatter plots showing PZ–HZ coherence as a function of (a,b) the water depth and (c,d) the PZ coherence of each member of a station pair for (a,c) 3–10 and (b,d) 15–30 s period. The gray shading is the same as in Figure 5. Note that we use the same plotting order as Figure 5 for direct comparison; that is, points with the highest ΔSNR values are plotted on top. The color version of this figure is available only in the electronic edition.

2 km layer of sediment on top of the upper oceanic crust. Surface-wave dispersion, eigenfunctions, and ellipticity values are calculated using the SURF96 software (Herrmann, 2013). Here, we define the relative polarity of the P and Z components such that a decrease in pressure due to an uplift in ground displacement results in a $\pm 180^\circ$ phase separation. Polarity conventions for DPG responses can differ, so we adjust these for consistency across deployments. Using this convention, the P and Z records of fundamental-mode Scholte and Rayleigh waves are out of phase, and the amplitude of the



TF (or admittance) is calculated as the ratio of the vertical displacement eigenfunction U_z to the vertical stress eigenfunction (proportional to the spatial gradient of displacement) τ_{zz} at the seafloor (Ruan *et al.*, 2014):

$$T_{ZP}(f) = \frac{U_z(f)}{\tau_{zz}(f)} = \frac{U_z(f)}{K \left[\frac{\partial U_x}{\partial x(f)} + \frac{\partial U_z}{\partial z(f)} \right]}, \quad (7)$$

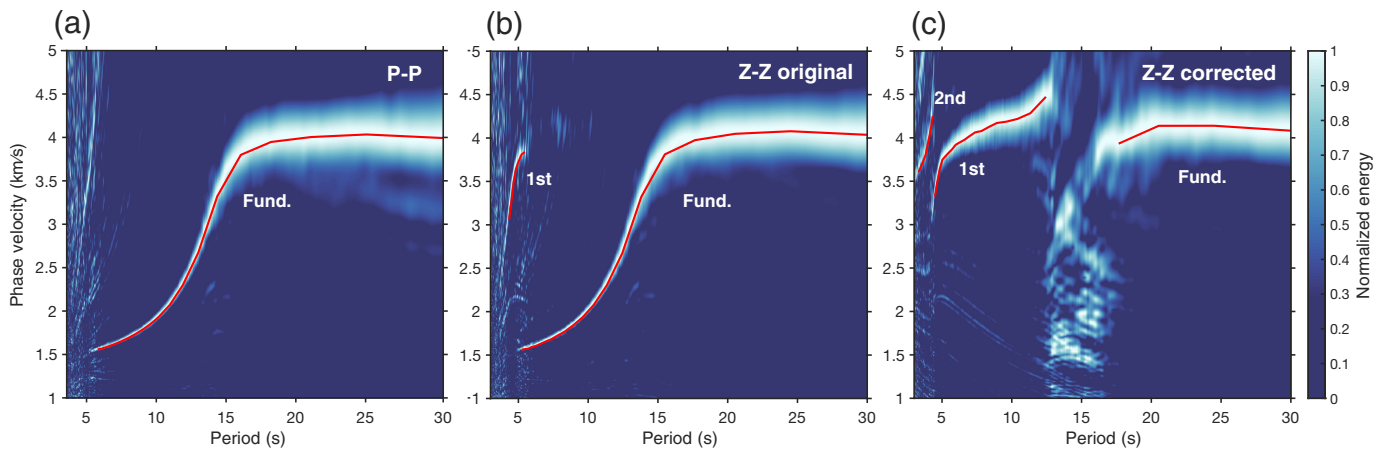
in which K is the incompressibility of water and U_x is the horizontal displacement eigenfunction.

Based on our synthetic tests, interface wave sensitivity strongly differs in the presence of thick sediments, resulting in differences in phase velocity dispersion, seafloor admittance, and wave ellipticity (Fig. 7). In the absence of sediments, the fundamental-mode Scholte wave is largely sensitive to the water column, as shown by the vertical displacement eigenfunctions (Fig. 7b). This wave is sometimes described as a leaky Rayleigh wave, distinguished from a Scholte wave on the basis of the subsurface shear velocity and wave ellipticity (Zhu and Popovics, 2006). Its sensitivity to the water column is reflected in the phase velocity dispersion, which approaches the acoustic water wavespeed (1.5 km/s) at periods <10 s (Fig. 7c). In contrast, the first-overtone Rayleigh wave samples deeper into the crust and uppermost mantle down to ~40 km depth, and phase

Figure 7. Synthetic Scholte and Rayleigh-wave calculations for a model containing no sediments (blue) and a model containing a 2-km-thick sediment layer (red). (a) Shear velocity model, (b) vertical displacement eigenfunctions at 6 s period, (c) phase velocity dispersion, (d) admittance, and (e) ellipticity. The fundamental mode and first overtone are indicated by solid and dashed lines, respectively. The color version of this figure is available only in the electronic edition.

velocities are 3.5–4.2 km/s at these periods. For thick sediments, the fundamental-mode Scholte-wave energy is trapped predominantly in the sediment layer (Fig. 7b), leading to phase velocities <1.5 km/s at short periods, approaching sediment shear velocity. The first overtone also shows significant sensitivity to the sediments as well as the upper crust, resulting in phase velocities that are comparable to that of the sediment-free fundamental Scholte mode at periods <10 s. Slower velocities and less separation of the mode branches in the presence of thick sediments implies potentially stronger overtone interference and hence more difficulty isolating mode branches.

To validate these findings, we analyzed real data from the NoMelt experiment, which features relatively thin sediments (~250 m; Mark *et al.*, 2019; Russell *et al.*, 2019), resembling the sediment-free model (Fig. 7). We apply a linear Radon transform to P-P and Z-Z CCFs to extract multimode



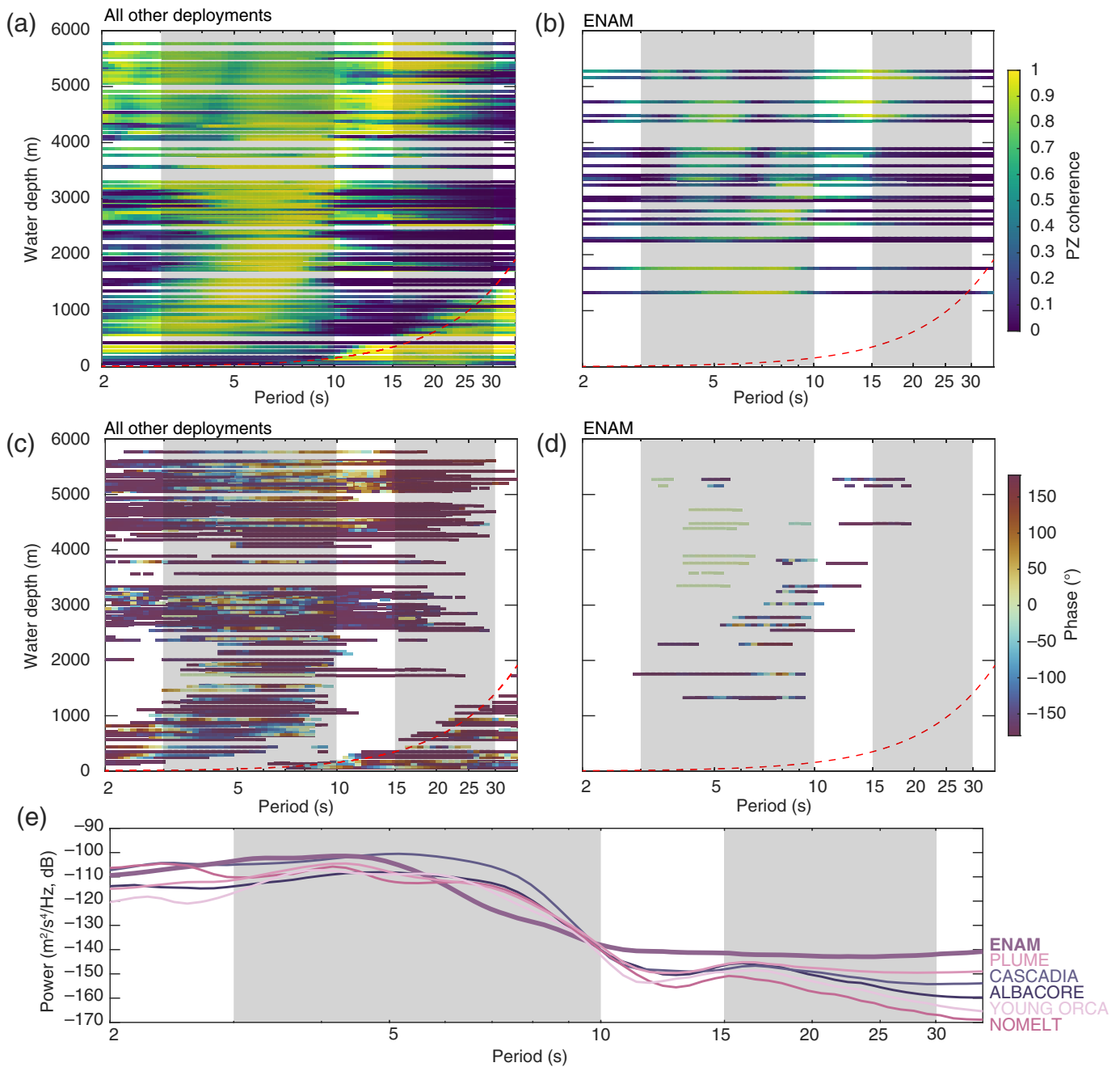
dispersion characteristics (Luo *et al.*, 2008, 2015; Russell, 2021; Fig. 8). In this setting, the P-P component captures only the fundamental-mode branch (Fig. 8a), whereas the original Z-Z component reveals both fundamental-mode and first-overtone energy (Fig. 8b). After applying TF corrections, the fundamental Scholte wave is removed from the Z-Z component, the first overtone becomes more prominent between ~ 5 and 12 s, and the second overtone emerges at periods < 5 s (Fig. 8c). These overtones are sensitive to the crust and shallow lithospheric mantle, and offer potential for high-resolution imaging. Although the second overtone has been observed in earlier studies (Russell, 2021; Phillips *et al.*, 2023), to our knowledge it has not yet been used for structural imaging of the oceanic lithosphere using passive broadband seismic arrays. Overall, the observed dispersion aligns well with predictions from the sediment-free model.

Unfortunately, a similar analysis for a deployment with thick sediments (i.e., ENAM) results in a Radon transform largely absent of distinct dispersion curves due to the poor quality of the CCFs, and heterogeneous water depth and sediment structure (Russell and Gaherty, 2021). However, noise properties of the ENAM deployment are consistent with higher-mode interference at 3–10 s period due to thick sediments. At deployments excluding ENAM, we observe high-PZ coherences over this band (Fig. 9a). At water depths $>\sim 4500$ m, distinct minima in PZ coherence are observed, although these are primarily restricted to periods < 5 s. Furthermore, coherence values remain $> \sim 0.5$ at these minima. In contrast, ENAM stations have lower overall PZ coherence values in this period band (Fig. 9b). Distinct coherence minima begin at ~ 3000 m water depth, reaching near-zero values. We also examine the phase relationship between the P and Z components as a function of period where the PZ coherence is > 0.7 . Excluding ENAM, the P and Z components are mostly directly out of phase ($\pm 180^\circ$), as expected given our polarity conventions (Fig. 9c). We observe scatter at some stations, particularly at periods with reduced coherences. These subsequently return to phase separations of $\pm 180^\circ$ at higher coherence values at most stations. In contrast, ENAM consistently shows a distinct

Figure 8. Linear Radon transform panels displaying array-average dispersion at the NoMelt deployment obtained from ambient noise CCFs. (a) P-P component, (b) original Z-Z component without TF corrections applied, and (c) corrected Z-Z component with TF corrections applied. Red lines indicate high-quality dispersion branches extracted from the Radon panels. The color version of this figure is available only in the electronic edition.

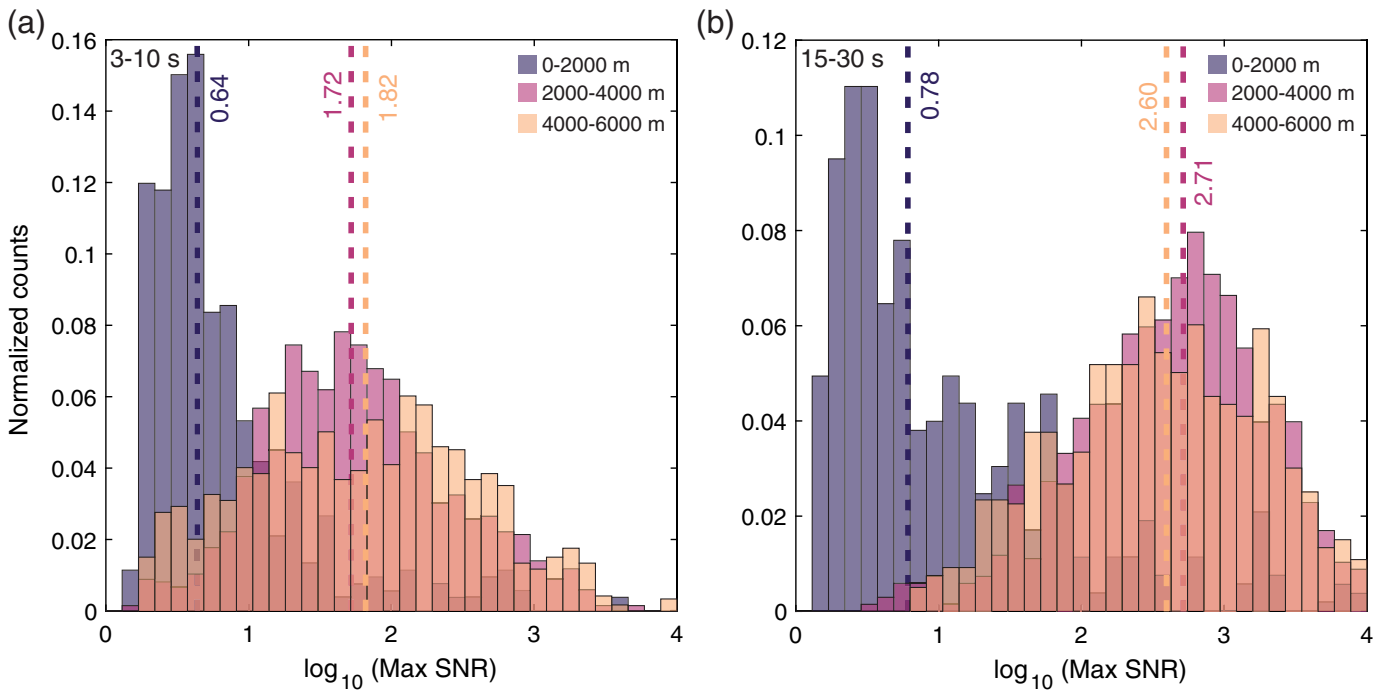
pattern of 180° phase flips as a function of period (Fig. 9d). At a single station, longer period high-PZ coherence peaks have a phase separation of $\pm 180^\circ$, followed by a flip to a phase of 0° at shorter periods. These phase flips are separated by the distinct minima in PZ coherence (Fig. 9b,d).

Significant decreases in PZ coherence at BBOBS at periods < 10 s, particularly accompanied by a $\pm 180^\circ$ change in phase, can indicate interference from higher order modes (Ruan *et al.*, 2014). This may also result from a transition from retrograde to prograde elliptical particle motion at the seafloor for the fundamental mode and first overtone. Onshore, fundamental-mode Rayleigh waves can exhibit prograde particle motion in the presence of very thick sedimentary layers with slow surface velocities (Tanimoto and Rivera, 2005). Similar observations for higher modes are also documented at sedimentary basins on land (Ma *et al.*, 2016; Nayak and Thurber, 2020). Changes from retrograde to prograde particle motion should be accompanied by sharp minima in ellipticity, as seen in our thick sediment model (Fig. 7e). Measurements of Rayleigh-wave ellipticity on BBOBS instruments are often hindered by high noise levels on horizontal components (Janiszewski *et al.*, 2023); thus, a detailed analysis is outside the scope of our current study. However, the ENAM observations are consistent with expectations for mode interference in the presence of thick sediments. Combined with their uniqueness relative to other deployments, and the anomalously thick sediments beneath ENAM, we suggest that complex particle motion and mode interference play a significant role in the CCFs of this deployment at periods < 10 s.



Additional environmental factors may also influence microseism amplitudes. For example, BBOBS in the Atlantic Ocean are expected to record weaker microseism signals at periods >7 s compared to those in the Pacific due to differences in wind regimes (Webb, 1992; Babcock *et al.*, 1994). We observe this pattern when comparing mean Z-component power spectra across deployments (Fig. 9e), excluding shallow-water (<500 m) stations, as these have distinct microseism noise characteristics (Webb, 1992; Janiszewski *et al.*, 2023). ENAM, located in the western Atlantic, indeed shows reduced secondary microseism energy at longer periods relative to Pacific deployments. Furthermore, ENAM's location within the strong Gulf Stream current likely contributes to its unique

Figure 9. P-Z coherence plotted as a function of broadband ocean-bottom seismometer (BBOBS) water depth for (a) all analyzed deployments excluding ENAM and (b) ENAM. P-Z phase relationship plotted as a function of BBOBS water depth for (c) all analyzed deployments excluding ENAM and (d) ENAM. Phase is only plotted at periods where PZ coherence exceeds 0.7. Individual horizontal lines represent a single BBOBS, gray shaded areas indicate the 3–10 and 15–30 s period bands, and the red-dashed line indicates the predicted infragravity cutoff as a function of water depth. (e) Average Z-component noise power spectral density functions calculated as the mean of each deployment. Stations with water depths shallower than 500 m are excluded. The color version of this figure is available only in the electronic edition.



noise environment (Russell and Gaherty, 2021), adding to the complexity of its seismic recordings.

Criteria for success

The effectiveness of TF corrections on ambient noise CCFs depends on environmental conditions and instrumentation. In the 3–10 s band, these corrections are most reliable at deep, open-ocean stations. Specifically, we observe that the first-overtone Rayleigh-wave signal is consistently enhanced for station pairs when both their mean water depth exceeds ~ 4000 m and PZ coherence is $> \sim 0.5$ (Fig. 3d). In all other cases, the impact of the TF corrections becomes less predictable. Under these conditions, it may be beneficial to compare CCFs before and after correction, and select the highest quality version for further analysis.

In the 15–30 s band, several important considerations arise. First, the PZ TF correction should only be applied at periods that are within the expected infragravity wave band for a given station's water depth. Applying it outside this range risks removing the fundamental-mode Rayleigh wave, which carries valuable structural information. Some studies have proposed using coherence thresholds to avoid such issues (e.g., Tian and Ritzwoller, 2017), and we emphasize the importance of distinguishing whether the observed coherence stems from microseism activity or infragravity waves. By contrast, tilt noise corrections show more variable outcomes across different settings. Although they can improve ΔSNR , their effect is not consistently tied to water depth or other environmental factors (Fig. S3, Fig. 6). This is likely due to the stronger relationship between tilt noise and instrumentation (Janiszewski *et al.*, 2023). Therefore, tilt corrections should be applied routinely,

Figure 10. Histograms of maximum CCF signal-to-noise ratios (SNRs; e.g., the maximum SNR out of the original and TF corrected CCF for each station pair) in the solid-velocity window grouped by water depth for the (a) 3–10 and (b) 15–30 s period band. Median values for each water depth group are shown by dashed lines. The color version of this figure is available only in the electronic edition.

but CCFs should be evaluated post-correction to confirm that data quality has improved. Overall, these findings suggest that no single preprocessing workflow will work equally well in all environments, especially outside of deep, open-ocean environments. Finally, thick sediments can significantly complicate short-period ambient noise analyses.

To evaluate the overall usability of ambient noise data, we examine the distribution of maximum SNR value of either the original or corrected CCFs across all station pairs (Fig. 10, Fig. S7). This approach does not distinguish cases for which tilt corrections alone might yield the highest SNRs, but it provides a general overview of data quality trends. As expected, SNR values are generally high, with $\sim 75\%$ of observations exceeding an SNR of 10 in the 3–10 s band and $\sim 89\%$ in the 15–30 s band. However, quality drops sharply for station pairs with mean water depths < 2000 m, where median SNRs fall to 4.4 (3–10 s) and 6.0 (15–30 s). In deeper waters, median SNRs exceed 50 and 400 in the respective bands. This contrast highlights that fewer sufficient-quality CCFs are likely in shallow water, although it is important to emphasize that the maximum range of SNRs for shallow water stations is similar to all water depths. In addition, SNR levels are consistently higher in

the 15–30 s band than in the 3–10 s band, especially at water depths >2000 m. This difference may reflect greater attenuation of shorter-period signals or increased noise contamination.

Conclusions

Systematic analysis of ambient noise CCFs across six BBOBS deployments demonstrates that water depth, sediment thickness, ocean basin characteristics, and instrumentation impact data quality and effectiveness of TF corrections. In the 15–30 s period band, signal quality is primarily governed by infragravity wave and tilt noise, which vary with water depth and instrument design, respectively. Applying TF corrections within the appropriate period bands for these noise sources improves CCFs, but using them outside these ranges can unintentionally remove the fundamental-mode Rayleigh wave, which is critical for structural imaging. These relationships likely continue at longer periods where tilt and compliance noise remain the dominant noise sources (Tian and Ritzwoller, 2017). In the 3–10 s period band, CCFs are shaped by the properties of the fundamental-mode Scholte wave and first-overtone Rayleigh wave. The velocities and period ranges of these waves are primarily related to water depth and sediment structure.

Our results highlight both the challenges and opportunities in using ambient noise for imaging in marine environments, particularly at shorter periods. The results in the 3–10 s band emphasize that shallow structure significantly affects how interface waves propagate, influencing the success of ambient noise techniques traditionally used to image deeper crustal and lithospheric structure. Covariance of environmental and deployment parameters remains a persistent barrier to isolate relationships, and viable directions for future research may include analysis of non-US-led deployments or targeted pilot deployments to better quantify the role of specific variables (Janiszewski *et al.*, 2023). It is notable that Janiszewski *et al.* (2023) do not find a significant relationship between sediment thickness and BBOBS noise properties, likely due to their broad focus on periods longer than 1 s. Our CCF results demonstrate that bandlimited investigations motivated by specific use cases for BBOBS data can yield additional insights, further clarifying directions for future investigations.

Our results also demonstrate that at 3–10 s interface waves can be highly sensitive to the water column and shallow sediment structure, potentially representing relatively novel directions for broadband ambient noise imaging studies. Scholte waves are more commonly analyzed to constrain sediment velocities in marine active-source experiments and typically use periods shorter than 1 s facilitated by denser instrument spacing than passive, broadband arrays (Nolet and Dorman, 1996; Bohlen *et al.*, 2004; Kugler *et al.*, 2007; Nguyen *et al.*, 2009). Recent ocean-bottom nodal and DAS deployments show that ambient noise generated Scholte waves can also image the sedimentary layer, in some cases extending to

periods >1 s (Tomar *et al.*, 2016; Lior *et al.*, 2022; Girard *et al.*, 2024). Developments in long-term seafloor cabled observations (e.g., Kelley *et al.*, 2014; Shinohara *et al.*, 2021; Howe *et al.*, 2022) open additional opportunities for monitoring changes in seismic velocity over time using ambient noise observations. Such techniques typically focus on periods from ~0.25 to 10 s (Lee *et al.*, 2024), overlapping with the band where we observe complex interface wave properties. The overlap of these diverse approaches suggests that further exploration of the utilization of both Scholte and Rayleigh waves in passive, broadband ambient noise imaging studies may yield new insights. However, our results demonstrate that leveraging both Scholte and Rayleigh waves will require careful identification of different mode branches and modeling of depth sensitivities. Although simple 1D modeling approaches (e.g., Herrmann, 2013) yield useful insights, more computationally robust methodologies that incorporate 2D or 3D heterogeneity and better represent the full waveform may improve accuracy of interpretations. Addressing these challenges will be key to unlocking the full potential of ambient noise imaging in marine settings.

Data and Resources

The seismic and pressure time-series data are available for download through the EarthScope Data Management Center (DMC; <https://ds.iris.edu/ds/nodes/dmc/>) under the following network codes: 2D.2010, 7D.2011, XE.2018, YO.2014, YS.2004, and ZA.2011. The codes for broadband ocean-bottom seismometer (BBOBS) noise transfer function (TF) calculations and corrections are based on the MATLAB version (www.mathworks.com/products/matlab) of the ATaCR code part of the OBStool package (Audet and Janiszewski, 2020), and are available for download via GitHub (<https://github.com/helenjanisz/ATaCR>). A modified version of ATaCR used in this article for ambient noise applications can be found here: https://github.com/jbrussell/ATaCR/tree/correct_noise. Calculation of the ambient noise cross-correlation functions (CCFs) and array dispersion measurements uses the MATnoise code available for download via GitHub (<https://github.com/jbrussell/MATnoise>). All websites were last accessed in March 2025. The supplemental material contains figures of additional parameters and data separated by individual deployments.

Declaration of Competing Interests

The authors acknowledge that there are no conflicts of interest recorded.

Acknowledgments

The data analyzed herein were collected on instruments maintained by ocean-bottom seismic instrument center (OBSIC) and the ocean-bottom seismograph instrument pool (OBSIP), and in deployments supported by the University National Oceanographic Laboratory System (UNOLS) funded by the National Science Foundation (NSF). The facilities of EarthScope Consortium were used for access to waveforms, related metadata, and/or derived products used in this study. These services are funded through the NSF's Seismological Facility for the Advancement of Geoscience (SAGE) Award under Cooperative

Agreement EAR-1724509. Figures were made using the M_Map code package (Pawlowicz, 2020), and the Scientific Color Maps package (Crameri, 2018). The article benefited from conversations with Spahr Webb, Jim Gaherty, Nick Harmon, and Robert Dunn. The authors acknowledge the thoughtful contributions of two anonymous reviewers and the editor whose feedback greatly improved this article. This work was partially supported by funds from the Gordon and Betty Moore Foundation Award GBMF10787, and NSF Award EAR-1952702.

References

- Aderhold, K., R. Woodward, and A. Frassetto (2019). Ocean bottom seismography instrument pool, *Final Report*, doi: [10.5281/zenodo.3524424](https://doi.org/10.5281/zenodo.3524424).
- Adimah, N. I., and S. Padhy (2019). Ambient noise Rayleigh wave tomography across the Madagascar Island, *Geophys. J. Int.* **220**, no. 3, 1657–1676, doi: [10.1093/gji/ggz542](https://doi.org/10.1093/gji/ggz542).
- Adimah, N. I., Y. J. Tan, and J. B. Russell (2024). Shear-wave velocity structure of the Blanco oceanic transform fault zone, *Geophys. J. Int.* **239**, no. 2, 1287–1312, doi: [10.1093/gji/ggae318](https://doi.org/10.1093/gji/ggae318).
- Ardhuin, F., E. Stutzmann, M. Schimmel, and A. Mangeney (2011). Ocean wave sources of seismic noise, *J. Geophys. Res.* **116**, no. C9, doi: [10.1029/2011jc006952](https://doi.org/10.1029/2011jc006952).
- Ardhuin, F., L. Gaultier, and E. Stutzmann (2015). How ocean waves rock the Earth: Two mechanisms explain microseisms with periods 3 to 300 s, *Geophys. Res. Lett.* **42**, no. 3, 765–772, doi: [10.1002/2014gl062782](https://doi.org/10.1002/2014gl062782).
- Audet, P., and H. Janiszewski (2020). OBStools: Software for processing broadband ocean-bottom seismic data, *Zenodo*, doi: [10.5281/zenodo.3905412](https://doi.org/10.5281/zenodo.3905412).
- Babcock, J. M., B. A. Kirkendall, and J. A. Orcutt (1994). Relationships between ocean bottom noise and the environment, *Bull. Seismol. Soc. Am.* **84**, no. 6, 1991–2007, doi: [10.1785/bssa0840061991](https://doi.org/10.1785/bssa0840061991).
- Bell, S. W., D. W. Forsyth, and Y. Ruan (2015). Removing noise from the vertical component records of ocean-bottom seismometers: Results from year one of the Cascadia initiative, *Bull. Seismol. Soc. Am.* **105**, no. 1, 300–313, doi: [10.1785/0120140054](https://doi.org/10.1785/0120140054).
- Bensen, G. D., M. H. Ritzwoller, M. P. Barmin, A. L. Levshin, F. Lin, M. P. Moschetti, N. M. Shapiro, and Y. Yang (2007). Processing seismic ambient noise data to obtain reliable broad-band surface wave dispersion measurements, *Geophys. J. Int.* **169**, no. 3, 1239–1260.
- Bohlen, T., S. Kugler, G. Klein, and F. Theilen (2004). 1.5D inversion of lateral variation of Scholte-wave dispersion Scholte-wave inversion, *Geophysics* **69**, no. 2, 330–344, doi: [10.1190/1.1707052](https://doi.org/10.1190/1.1707052).
- Bowden, D. C., M. D. Kohler, V. C. Tsai, and D. S. Weeraratne (2016). Offshore Southern California lithospheric velocity structure from noise cross-correlation functions, *J. Geophys. Res.* doi: [10.1002/2016jb012919](https://doi.org/10.1002/2016jb012919).
- Crameri (2018). Scientific colour maps, *Zenodo*, doi: [10.5281/zenodo.1243862](https://doi.org/10.5281/zenodo.1243862).
- Crawford, W. C., and S. C. Webb (2000). Identifying and removing tilt noise from low-frequency (<0.1Hz) Seafloor vertical seismic data, *Bull. Seismol. Soc. Am.* 952–963.
- Crawford, W. C., S. C. Webb, and J. A. Hildebrand (1991). Seafloor compliance observed by long-period pressure and displacement measurements, *J. Geophys. Res.* **96**, no. B10, 16,151–16,160, doi: [10.1029/91jb01577](https://doi.org/10.1029/91jb01577).
- Crawford, W. C., S. C. Webb, and J. A. Hildebrand (1998). Estimating shear velocities in the oceanic crust from compliance measurements by two-dimensional finite difference modeling, *J. Geophys. Res.* **103**, no. B5, 9895–9916, doi: [10.1029/97jb03532](https://doi.org/10.1029/97jb03532).
- Doran, A. K., and G. Laske (2020). Melt-affected ocean crust and uppermost mantle near Hawaii—Clues from ambient-noise phase velocity and seafloor compliance, *Geophys. J. Int.* **224**, no. 2, 843–857, doi: [10.1093/gji/ggaa470](https://doi.org/10.1093/gji/ggaa470).
- Eilon, Z. C., J. B. Gaherty, L. Zhang, J. Russell, S. McPeak, J. Phillips, D. W. Forsyth, and G. Ekström (2021). The Pacific OBS Research into Convecting Asthenosphere (ORCA) experiment, *Seismol. Res. Lett.* **93**, no. 1, 477–493, doi: [10.1785/0220210173](https://doi.org/10.1785/0220210173).
- Girard, A. J., J. Shragge, M. Danilouchkine, C. Udengaard, and S. Gerritsen (2024). Observations from the seafloor: Ultra-low-frequency ambient ocean-bottom nodal seismology at the Amendment field, *Geophys. J. Int.* **239**, no. 1, 17–36, doi: [10.1093/gji/ggaa249](https://doi.org/10.1093/gji/ggaa249).
- Hable, S., K. Sigloch, E. Stutzmann, S. Kiselev, and G. Barruol (2019). Tomography of crust and lithosphere in the western Indian Ocean from noise cross-correlations of land and ocean bottom seismometers, *Geophys. J. Int.* **219**, no. 2, 924–944, doi: [10.1093/gji/ggz333](https://doi.org/10.1093/gji/ggz333).
- Harmon, N., D. Forsyth, and S. Webb (2007). Using ambient seismic noise to determine short-period phase velocities and shallow shear velocities in young oceanic lithosphere, *Bull. Seismol. Soc. Am.* **97**, no. 6, 2009–2023, doi: [10.1785/0120070050](https://doi.org/10.1785/0120070050).
- Herrmann, R. B. (2013). Computer programs in seismology: An evolving tool for instruction and research, *Seismol. Res. Lett.* **84**, no. 6, 1081–1088, doi: [10.1785/0220110096](https://doi.org/10.1785/0220110096).
- Howe, B. M., M. Angove, J. Aucan, C. R. Barnes, J. S. Barros, N. Bayliff, N. C. Becker, F. Carrilho, M. J. Fouch, B. Fry, et al. (2022). SMART subsea cables for observing the earth and ocean, mitigating environmental hazards, and supporting the blue economy, *Front. Earth Sci.* **9**, doi: [10.3389/feart.2021.775544](https://doi.org/10.3389/feart.2021.775544).
- Janiszewski, H. A., J. B. Gaherty, G. A. Abers, H. Gao, and Z. C. Eilon (2019). Amphibious surface-wave phase-velocity measurements of the Cascadia subduction zone, *Geophys. J. Int.* **217**, no. 3, 1929–1948, doi: [10.1093/gji/ggz051](https://doi.org/10.1093/gji/ggz051).
- Janiszewski, H. A., Z. Eilon, J. B. Russell, B. Brunsvik, J. B. Gaherty, S. G. Mosher, W. B. Hawley, and S. Coats (2023). Broad-band ocean bottom seismometer noise properties, *Geophys. J. Int.* **233**, no. 1, 297–315, doi: [10.1093/gji/ggac450](https://doi.org/10.1093/gji/ggac450).
- Kawano, Y., T. Isse, A. Takeo, H. Kawakatsu, M. Morishige, H. Shiobara, N. Takeuchi, H. Sugioka, Y. Kim, H. Utada, et al. (2023). Seismic structure of the lithosphere–asthenosphere system beneath the oldest seafloor revealed by Rayleigh-wave dispersion analysis, *J. Geophys. Res.* **128**, no. 6, doi: [10.1029/2023jb026529](https://doi.org/10.1029/2023jb026529).
- Kelley, D. S., J. R. Delaney, and S. K. Juniper (2014). Establishing a new era of submarine volcanic observatories: Cabling axial seamount and the Endeavour segment of the Juan de Fuca Ridge, *Mar. Geol.* **352**, 426–450, doi: [10.1016/j.margeo.2014.03.010](https://doi.org/10.1016/j.margeo.2014.03.010).
- Kugler, S., T. Bohlen, T. Forbriger, S. Bussat, and G. Klein (2007). Scholte-wave tomography for shallow-water marine sediments, *Geophys. J. Int.* **168**, no. 2, 551–570, doi: [10.1111/j.1365-246x.2006.03233.x](https://doi.org/10.1111/j.1365-246x.2006.03233.x).
- Le, B. M., T. Yang, Y. J. Chen, and H. Yao (2017). Correction of OBS clock errors using Scholte waves retrieved from cross-correlating hydrophone recordings, *Geophys. J. Int.* **212**, no. 2, 891–899, doi: [10.1093/gji/ggx449](https://doi.org/10.1093/gji/ggx449).

- Lee, M. K., Y. J. Tan, J. B. Russell, M. Tolstoy, and F. Waldhauser (2024). Relative seismic velocity variations at axial seamount observed with ambient seismic noise capture transition point in volcanic inflation, *Geophys. Res. Lett.* **51**, no. 10, doi: [10.1029/2024gl108883](https://doi.org/10.1029/2024gl108883).
- Lin, F., M. D. Kohler, P. Lynett, A. Ayca, and D. S. Weeraratne (2015). The 11 March 2011 Tohoku tsunami wave front mapping across offshore Southern California, *J. Geophys. Res.* **120**, no. 5, 3350–3362, doi: [10.1002/2014jb011524](https://doi.org/10.1002/2014jb011524).
- Lin, P.-Y. P., J. B. Gaherty, G. Jin, J. A. Collins, D. Lizarralde, R. L. Evans, and G. Hirth (2016). High-resolution seismic constraints on flow dynamics in the oceanic asthenosphere, *Nature* **535**, no. 7613, 538–541, doi: [10.1038/nature18012](https://doi.org/10.1038/nature18012).
- Lior, I., E. D. Mercrat, D. Rivet, A. Sladen, and J.-P. Ampuero (2022). Imaging an underwater basin and its resonance modes using optical fiber distributed acoustic sensing, *Seismol. Res. Lett.* **93**, no. 3, 1573–1584, doi: [10.1785/0220210349](https://doi.org/10.1785/0220210349).
- Luo, Y., J. Xia, R. D. Miller, Y. Xu, J. Liu, and Q. Liu (2008). Rayleigh-Wave dispersive energy imaging using a high-resolution linear radon transform, *Pure Appl. Geophys.* **165**, no. 5, 903–922, doi: [10.1007/s00024-008-0338-4](https://doi.org/10.1007/s00024-008-0338-4).
- Luo, Y., Y. Yang, Y. Xu, H. Xu, K. Zhao, and K. Wang (2015). On the limitations of interstation distances in ambient noise tomography, *Geophys. J. Int.* **201**, no. 2, 652–661, doi: [10.1093/gji/ggv043](https://doi.org/10.1093/gji/ggv043).
- Lynner, C., J. A. Van Avendonk, H. Bécel, A. Christeson, G. L. Dugan, B. Gaherty, J. B. Harder, S. Hornbach, M. J. Lizarralde, D. Long, et al. (2019). The Eastern North American margin community seismic experiment: An amphibious active- and passive-source dataset, *Seismol. Res. Lett.* **91**, no. 1, 533–540, doi: [10.1785/0220190142](https://doi.org/10.1785/0220190142).
- Ma, Y., R. W. Clayton, and D. Li (2016). Higher-mode ambient-noise Rayleigh waves in sedimentary basins, *Geophys. J. Int.* **206**, no. 3, 1634–1644, doi: [10.1093/gji/ggw235](https://doi.org/10.1093/gji/ggw235).
- Mark, H. F., D. Lizarralde, J. A. Collins, N. C. Miller, G. Hirth, J. B. Gaherty, and R. L. Evans (2019). Azimuthal seismic anisotropy of 70-Ma Pacific-plate upper mantle, *J. Geophys. Res.* **79**, no. 26, 4011–4021, doi: [10.1029/2018jb016451](https://doi.org/10.1029/2018jb016451).
- McNamara, D. E., and R. P. Buland (2004). Ambient noise levels in the Continental United States, *Bull. Seismol. Soc. Am.* **94**, no. 4, 1517–1527, doi: [10.1785/0120030001](https://doi.org/10.1785/0120030001).
- Nayak, A., and C. H. Thurber (2020). Using multicomponent ambient seismic noise cross-correlations to identify higher mode Rayleigh waves and improve dispersion measurements, *Geophys. J. Int.* **222**, no. 3, 1590–1605, doi: [10.1093/gji/ggaa270](https://doi.org/10.1093/gji/ggaa270).
- Nguyen, X. N., T. Dahm, and I. Grevemeyer (2009). Inversion of Scholte wave dispersion and waveform modeling for shallow structure of the Ninety east Ridge, *J. Seismol.* **13**, no. 4, 543–559, doi: [10.1007/s10950-008-9145-8](https://doi.org/10.1007/s10950-008-9145-8).
- Nolet, G., and L. M. Dorman (1996). Waveform analysis of Scholte modes in ocean sediment layers, *Geophys. J. Int.* **125**, no. 2, 385–396, doi: [10.1111/j.1365-246x.1996.tb00006.x](https://doi.org/10.1111/j.1365-246x.1996.tb00006.x).
- Pawlowicz, R. (2020). M_Map: A mapping package for MATLAB, version 1.4m, available at www.eoas.ubc.ca/~rich/map.html (last accessed March 2025).
- Phillips, J., J. Gaherty, J. Russell, Z. Eilon, D. Forsyth, and J. Byrnes (2023). Spatial variation in anisotropic shear velocity of old oceanic lithosphere-asthenosphere in the southwest pacific, AGU Fall Meeting Abstracts, San Francisco, California.
- Pinzón, J. I., S. Custódio, G. Silveira, F. Krüger, J. Mata, and L. Matias (2023). Crustal and uppermost mantle structure near the Gloria Fault, North Atlantic, from ocean bottom seismometer surface wave observations, *Geophys. J. Int.* **236**, no. 1, 1–13, doi: [10.1093/gji/ggad405](https://doi.org/10.1093/gji/ggad405).
- Ruan, Y., D. W. Forsyth, and S. Bell (2014). Marine sediment shear velocity structure from the ratio of displacement to pressure of Rayleigh waves at seafloor, *J. Geophys. Res.* doi: [10.1002/\(issn\)2169-9356](https://doi.org/10.1002/(issn)2169-9356).
- Russell, J. B., and J. B. Gaherty (2021). Lithosphere structure and seismic anisotropy offshore Eastern North America: Implications for continental breakup and ultra-slow spreading dynamics, *J. Geophys. Res.* **126**, no. 12, doi: [10.1029/2021jb022955](https://doi.org/10.1029/2021jb022955).
- Russell, J. B., J. B. Gaherty, H. F. Mark, G. Hirth, L. N. Hansen, D. Lizarralde, J. A. Collins, and R. L. Evans (2022). Seismological evidence for girdled olivine lattice-preferred orientation in oceanic lithosphere and implications for mantle deformation processes during seafloor spreading, *Geochem. Geophys. Geosys.* **23**, no. 10, doi: [10.1029/2022gc010542](https://doi.org/10.1029/2022gc010542).
- Russell, J. B., J. B. Gaherty, P.-Y. P. Lin, D. Lizarralde, J. A. Collins, G. Hirth, and R. L. Evans (2019). High-resolution constraints on Pacific Upper Mantle Petrofabric inferred from surface-wave anisotropy, *J. Geophys. Res.* **124**, no. 1, 631–657, doi: [10.1029/2018jb016598](https://doi.org/10.1029/2018jb016598).
- Russell, J. B. (2021). Structure and evolution of the oceanic lithosphere-asthenosphere system from high-resolution surface-wave imaging, *Ph.D. Thesis*, Columbia University, doi: [10.7916/d8-33w6-f908](https://doi.org/10.7916/d8-33w6-f908).
- Scholte, J. G. (1947). The range of existence of Rayleigh and Stoneley waves, *Geophys. J. Int.* **5**, 120–126, doi: [10.1111/j.1365-246x.1947.tb00347.x](https://doi.org/10.1111/j.1365-246x.1947.tb00347.x).
- Shapiro, N. M., and M. Campillo (2004). Emergence of broadband Rayleigh waves from correlations of the ambient seismic noise, *Geophys. Res. Lett.* **31**, no. 7, doi: [10.1029/2004gl019491](https://doi.org/10.1029/2004gl019491).
- Shinohara, M., T. Yamada, K. Uehira, S. Sakai, H. Shiobara, and T. Kanazawa (2021). Development and operation of an ocean bottom cable seismic and tsunami (OBCST) observation system in the source region of the Tohoku-Oki earthquake, *Earth Space Sci.* **8**, no. 3, doi: [10.1029/2020ea001359](https://doi.org/10.1029/2020ea001359).
- Straume, E. O., C. Gaina, S. Medvedev, K. Hochmuth, K. Gohl, J. M. Whittaker, R. Abdul Fattah, J. C. Doornenbal, and J. R. Hopper (2019). GlobSed: Updated total sediment thickness in the World's Oceans, *Geochem. Geophys. Geosys.* **20**, no. 4, 1756–1772, doi: [10.1029/2018gc008115](https://doi.org/10.1029/2018gc008115).
- Takeo, A., H. Kawakatsu, T. Isse, K. Nishida, H. Sugioka, A. Ito, H. Shiobara, and D. Suetsugu (2016). Seismic azimuthal anisotropy in the oceanic lithosphere and asthenosphere from broadband surface wave analysis of OBS array records at 60 Ma seafloor, *J. Geophys. Res.* **121**, no. 3, 1927–1947, doi: [10.1002/2015jb012429](https://doi.org/10.1002/2015jb012429).
- Takeo, A., D. W. Forsyth, D. S. Weeraratne, and K. Nishida (2014). Estimation of azimuthal anisotropy in the NW Pacific from seismic ambient noise in seafloor records, *Geophys. J. Int.* **199**, no. 1, 11–22, doi: [10.1093/gji/ggu240](https://doi.org/10.1093/gji/ggu240).
- Tanimoto, T., and L. Rivera (2005). Prograde Rayleigh wave particle motion, *Geophys. J. Int.* **162**, no. 2, 399–405, doi: [10.1111/j.1365-246x.2005.02481.x](https://doi.org/10.1111/j.1365-246x.2005.02481.x).
- Tian, Y., and M. H. Ritzwoller (2017). Improving ambient noise cross-correlations in the noisy ocean bottom environment of

- the Juan de Fuca plate, *Geophys. J. Int.* **210**, no. 3, 1787–1805, doi: [10.1093/gji/ggx281](https://doi.org/10.1093/gji/ggx281).
- Tomar, G., N. M. Shapiro, A. Mordret, S. C. Singh, and J.-P. Montagner (2016). Radial anisotropy in Valhall: Ambient noise-based studies of Scholte and Love waves, *Geophys. J. Int.* **208**, no. 3, 1524–1539, doi: [10.1093/gji/ggw480](https://doi.org/10.1093/gji/ggw480).
- Toomey, D., R. Allen, A. Barclay, S. Bell, P. Bromirski, R. Carlson, X. Chen, J. A. Collins, R. P. Dziak, B. Evers, *et al.* (2014). The Cascadia initiative: A sea change in seismological studies of subduction zones, *Oceanography* **27**, no. 2, 138–150, doi: [10.5670/oceanog.2014.49](https://doi.org/10.5670/oceanog.2014.49).
- Webb, S. C., and W. C. Crawford (2010). Shallow-Water_Broadband_OBS_Seismology.pdf, *Bull. Seismol. Soc. Am.* **100**, no. 4, 1770–1778, doi: [10.1785/0120090203](https://doi.org/10.1785/0120090203).
- Webb, S. C. (1992). The equilibrium oceanic microseism spectrum, *J. Acoust. Soc. Am.* **92**, no. 4, 2141–2158, doi: [10.1121/1.405226](https://doi.org/10.1121/1.405226).
- Webb, S. C. (1998). Broadband seismology and noise under the ocean, *Rev. Geophys.* **36**, no. 1, 105–142.
- Williams, E. F., M. R. Fernández-Ruiz, R. Magalhaes, R. Vanthillo, Z. Zhan, M. González-Herráez, and H. F. Martins (2019). Distributed sensing of microseisms and teleseisms with submarine dark fibers, *Nat. Commun.* **10**, no. 1, 5778, doi: [10.1038/s41467-019-13262-7](https://doi.org/10.1038/s41467-019-13262-7).
- Wolf, F. N., D. Lange, A. Dannowski, M. Thorwart, W. Crawford, L. Wiesenberg, I. Grevemeyer, and H. Kopp (2021). 3D crustal structure of the Ligurian Basin revealed by surface wave tomography using ocean bottom seismometer data, *Solid Earth* **12**, no. 11, 2597–2613, doi: [10.5194/se-12-2597-2021](https://doi.org/10.5194/se-12-2597-2021).
- Wolfe, C. J., S. C. Solomon, G. Laske, J. A. Collins, R. S. Detrick, J. A. Orcutt, D. Bercovici, and E. H. Hauri (2009). Mantle shear-wave velocity structure beneath the Hawaiian hot spot, *Science* **326**, no. 5958, 1388–1390, doi: [10.1126/science.1180165](https://doi.org/10.1126/science.1180165).
- Yang, X., Y. Luo, H. Xu, and K. Zhao (2020). Shear wave velocity and radial anisotropy structures beneath the central Pacific from surface wave analysis of OBS records, *Earth Planet. Sci. Lett.* **534**, 116086, doi: [10.1016/j.epsl.2020.116086](https://doi.org/10.1016/j.epsl.2020.116086).
- Yao, H., P. Gouédard, J. A. Collins, J. J. McGuire, and R. D. van der Hilst (2011). Structure of young East Pacific Rise lithosphere from ambient noise correlation analysis of fundamental- and higher-mode Scholte-Rayleigh waves, *C. R. Geosci.* **343**, nos. 8/9, 571–583, doi: [10.1016/j.crte.2011.04.004](https://doi.org/10.1016/j.crte.2011.04.004).
- Yeck, W. L., A. F. Sheehan, J. C. Stachnik, and F.-C. Lin (2017). Offshore Rayleigh group velocity observations of the South Island, New Zealand, from ambient noise data, *Geophys. J. Int.* **209**, no. 2, 827–841, doi: [10.1093/gji/gjx054](https://doi.org/10.1093/gji/gjx054).
- Zhu, J., and J. S. Popovics (2006). Analytical study of excitation and measurement of fluid-solid interface waves, *Geophys. Res. Lett.* **33**, L09603, doi: [10.1029/2006GL026068](https://doi.org/10.1029/2006GL026068).

Manuscript received 25 March 2025

Published online 16 September 2025